Structure, magnetism, and electronic properties in $3d$-$5d$ based double perovskite $(Sr_{1-x}Ca_x)_2FeIrO_6$ ($0 \leqslant x \leqslant 1$)

K. C. Kharkwal,[1] Roumita Roy,[2] Harish Kumar,[1] A. K. Bera[3], S. M. Yusuf[3,6] A. K. Shukla,[4] Kranti Kumar,[5]
Sudipta Kanungo[2,*] and A. K. Pramanik[1,†]

[1]*School of Physical Sciences, Jawaharlal Nehru University, New Delhi - 110067, India*
[2]*School of Physical Sciences, Indian Institute of Technology Goa, Goa - 403401, India*
[3]*Solid State Physics Division, Bhabha Atomic Research Centre, Mumbai - 400085, India*
[4]*National Physical Laboratory, Dr. K.S. Krishnan Road, New Delhi - 110012, India*
[5]*UGC-DAE Consortium for Scientific Research, Indore - 452001, India*
[6]*Homi Bhabha National Institute, Anushaktinagar, Mumbai - 400094, India*

The $3d$-$5d$ based double perovskites offer an ideal playground to study the interplay between electron correlation (U) and spin-orbit coupling (SOC) effect, showing exotic physics. The Sr_2FeIrO_6 is an interesting member in this family with ionic distribution of Fe^{3+} ($3d^5$) and Ir^{5+} ($5d^4$) where the later is believed to be nonmagnetic under the picture of strong SOC. Here we report a detailed investigation of structural, magnetic, and electronic transport properties along with electronic structure calculations in $(Sr_{1-x}Ca_x)_2FeIrO_6$ series with x from 0 to 1. While the basic interactions such as U and SOC are unlikely to be modified, a structural modification is expected due to ionic size difference between Sr^{2+} and Ca^{2+} which would influence other properties such as crystal field effect and bandwidths. While nonmonotonic changes in lattice parameters are observed across the series, the spectroscopic investigations reveal that $3+/5+$ charge state of Fe/Ir continue till the end of the series. An analysis of magnetic data suggests similar nonmonotonic evolution of magnetic parameters with doping. Temperature dependent crystal structure as well as low temperature (5 K) magnetic structure have been determined from neutron powder diffraction measurements which further indicate site ordered moments for both Fe and Ir. The whole series shows insulating behavior with a nonmonotonic variation in resistivity where the charge transport follows the three-dimensional variable range hopping model. The electronic structure calculations show, SOC enhanced, a noncollinear antiferromagnetic and a Mott-type insulating state is the stable ground state for the present series with a substantial amount of orbital moment, but less than the spin magnetic moment, at the Ir site and the magnetocrystalline anisotropy. The calculations further show the evolution of the spin and orbital magnetic moment components across the series along with the magnetization density. The obtained results imply that the local structural modification with introduction of lower size Ca^{2+} has a large influence on the magnetic and transport properties, further showing a large agreement between experimental results as well as theoretical calculations.

I. INTRODUCTION

An alternatively arranged, two interpenetrating face centered cubic (fcc) sublattices of B and B' transition metal cations govern most of the physical properties in double perovskites (DPs) with chemical composition $A_2BB'O_6$ where A is alkaline or rare-earth element [1–3]. The B and B' are generally octahedrally coordinated with the oxygen anions. The magnetic character of transition metal cations plays an important role as it introduces geometrical frustration that arises due to corner shared tetrahedra of either B or B' in the fcc sublattices. The sizes of the A, B, and B' cations further decide the structural stability of the DPs [4,5]. Mismatch in the sizes of cations distort the crystal structure to lower symmetry and this mismatch is conventionally measured using tolerance

factor (t),

$$t = \frac{r_A + r_O}{\sqrt{2}[(r_B + r_{B'})/2 + r_O]}, \quad (1)$$

where r_i is the respective ionic radii of A, B, B', and O ions [4,5]. With lowering of t, the most commonly occurred tilt systems in DPs are $Fm-3m \rightarrow I4/m \rightarrow I2/m \rightarrow P2_1/m \rightarrow I\bar{1}$. The tilt in structural symmetry leads to modification in magnetic and transport properties in these materials accordingly [4,5].

In DPs there are several choices for an A-site atom starting from an alkaline to rare-earth element [5]. Changes in valence state or ionic size of an A-site cation play a crucial role in tuning of magnetic as well as electronic properties [5]. For instance, substitution of smaller size Ca^{+2} for Sr^{2+} introduces local structural distortion which even distorts the crystal structure to lower symmetry, where the various magnetic ground states with different electronic properties are realized. A prominent

*sudipta@iitgoa.ac.in
†akpramanik@mail.jnu.ac.in

example is Sr_2FeReO_6, where introduction of Ca^{2+} not only drives the system from a metallic to an insulating state [6], but also diverse magnetic states such as spin glass (SG) or antiferromagnetic (AFM) have been found [7–9]. Previous studies have further shown a tetragonal structure with AFM ground state in Sr_2FeOsO_6, whereas Ca_2FeOsO_6 shows a distorted monoclinic structure and ferromagnetic (FM) state with a high transition temperature [10–12]. Interesting properties have also been observed in materials other than DPs. For instance, a suppression of FM state and resultant "quantum phase transition" have been observed in perovskite $Sr_{1-x}Ca_xRuO_3$ [13–15]. Further interesting results include spin configuration change in $(Sr_{1-x}Ca_x)_3YCo_4O_{10.5}$ [16], redistribution of charge along chains in $Sr_{14-x}Ca_xCu_{24}O_{41}$, suppression of anisotropic magnetoresistance in $La_{0.67}(Ca_{1-x}Sr_x)_{0.33}MnO_3$ [17–19], crossover from FM and Fermi liquid to AFM and metallic state in $Sr_{1-x}Ca_xCo_2P_2$ [20], etc.

The $3d$-$5d$ based DPs are of recent interest where many exotic states of matter may emerge due to fine interplay between electronic correlation (U) and spin-orbit coupling (SOC) which are prominent in $3d$ and $5d$ elements, respectively [21–26]. Iridium is one of the important choices for a $5d$ element because of its strong SOC and complex oxidation states ($4 + /5+$) [27–31]. Within the oxygen environment, the d orbitals of Ir split into e_g and t_{2g} states where the t_{2g} state under the influence of strong SOC further splits into a low lying $J_{eff} = 3/2$ quartet and a $J_{eff} = 1/2$ doublet. Following this model, a full-filled $J_{eff} = 3/2$ and a half-filled $J_{eff} = 1/2$ state is realized for Ir^{4+} ($5d^5$). The $J_{eff} = 1/2$ band, even in the presence of small U, opens up a gap around 0.5 eV, thus representing an exotic example of $J_{eff} = 1/2$ Mott insulator [27,28]. The Ir^{5+} ($5d^4$), on the other hand, has an empty $J_{eff} = 1/2$ state, therefore it is considered to have a nonmagnetic ground state ($J_{eff} = 0$) [32]. However, the emergence of SOC driven J_{eff} states is under debate. The breakdown of a J_{eff} picture in iridates under strong noncubic crystal field in the distorted IrO_6 octahedra has been reported for both Ir^{4+} and Ir^{5+} systems. For example, the Ir^{4+} systems, viz. $CaIrO_3$, Sr_2CeIrO_6, are the examples of the breakdown of a strong $J_{eff} = 1/2$ picture [33,34]. On the other side, the breakdown of $J_{eff} = 0$ state in Ir^{5+} has been evidenced by emergence of a nonzero magnetic moment in prototype systems of Sr_2YIrO_6, Ba_2YIrO_6, and $Ba_3ZnIr_2O_9$ [31,35–38]. An excitation from $J = 0$ (singlet) to low lying $J = 1$ (triplet) and 2 (quintet) states are expected to provide exotic magnetism in d^4 systems theoretically, however, recent moment dependent resonant inelastic x-ray scattering (RIXS) spectra analysis reveal that these low lying states are unlikely since the exchange strength between Ir-Ir is not sufficiently high to overcome the magnetic gap [39,40]. These suggest the origin of magnetism in iridium is still not very clear and needs further investigations in other similar materials.

In the present work we have studied detailed structural, magnetic, and electronic transport properties of $3d$-$5d$ based DPs $(Sr_{1-x}Ca_x)_2FeIrO_6$ ($0 \leqslant x \leqslant 1$). We have further done band structure calculations to understand the evolution of magnetic and electronic structure in the present series. The ionic sizes of Sr^{2+} and Ca^{+2} are 1.44 and 1.34 Å (12 coordination number), and those of Fe^{3+} (high spin state) and Ir^{5+} are 0.645 and 0.57 Å (6 coordination number), respectively

[41]. These reasonable differences between the ionic radii and charge states of transition metals would minimize the antisite disorder (i.e., occupation of Fe site by Ir and vice versa). The substitution of isoelectronic Ca^{2+} for Sr^{2+} will not tune the vital parameters such as SOC and U, but is expected to introduce (local) structural distortion through modification of bond length and bond angle between transition metals and oxygen. Therefore, the environment of individual FeO_6/IrO_6 octahedra will be modified which would affect the three-dimensional network of Fe-O-Ir-O-Fe. The introduced structural distortion with modified bandwidth will eventually compete with the other electronic energy scales (such as SOC and U), and based on its strength would introduce anisotropy, orbital magnetism, spin canting or even spin state transition in transition metals, etc. These will have large ramification on the magnetic and transport properties given that transition metal oxides exhibit prominent interrelation between lattice, spin, charge, and orbital degrees of freedom. The results will further help us to understand whether a conventionally accepted $J_{eff} = 0$ state for Ir^{5+} ($5d^4$) still remains valid in distorted crystal structure. Therefore, our interest is to investigate how the properties evolve from one end ($x = 0$) to the other end ($x = 1$) in the present series while the driving parameter is the structural distortion introduced by an ionic size mismatch. Furthermore, the whole series ($x = 0$ to 1) has been studied to examine any nonmonotonic evolution of parameters, as observed in other similar series [13,15,20].

The Sr_2FeIrO_6 ($x = 0$) shows a triclinic ($I\bar{1}$) or monoclinc ($P2_1/n$, $I2/m$) crystal structure and a long-range AFM-type transition around 120 K [42–46]. In our previous study [29] we have shown two magnetic transitions in Sr_2FeIrO_6; one prominent transition at ~45 K and another weak one at ~120 K. The similar dual AFM transitions with different spin structure are observed in other $3d$-$5d$ based DPs Sr_2FeOsO_6 [47,48]. Another end compound Ca_2FeIrO_6 ($x = 1$) has been shown to have monoclinc ($P2_1/n$) structure and a low temperature AFM transition at ~75 K [44]. Our structural investigation reveals that while the original crystal symmetry is retained across the series, the lattice parameters modify over the series. Spectroscopic analysis indicate a $3 + /5+$ charge state for Fe/Ir is retained over the series. In fact, we find that the structural, magnetic, and electronic parameters exhibit not only a nonmonotonic evolution with Ca (x) but their variations are correlated. The band structure calculations predict an AFM-insulating phase is the stable ground state in these materials under the combined influence of U and SOC. Furthermore, an evolution of magnetic moment component (m_x, m_y, m_z) with Ca concentration is predicted which mainly arises due to local structural distortion. Importantly, both the neutron measurements and the calculation show an agreement for the moment of Ir.

II. EXPERIMENTAL DETAILS

Polycrystalline samples of $(Sr_{1-x}Ca_x)_2FeIrO_6$ ($x = 0.0$, 0.05, 0.1, 0.2, 0.4, 0.6, 0.8, 1.0) series are prepared using solid state reaction method by calcination and sintering in high temperatures. The high purity ingredient powders (M/s Sigma Aldrich) of $SrCO_3$, $CaCO_3$, Fe_2O_3, and IrO_2 are taken in stoichiometric ratio and ground well. The ground fine powders are calcined in air at 900 °C for 24 h twice with an intermediate

grinding. Calcined powders are then pressed into pellets and sintered in air at 1000, 1050, and 1100 °C for 24 h each time with intermediate grindings. A horizontal tube furnace has been used for high temperature treatment. Given that IrO_2 is volatile in high temperature, a relatively low temperature required for the present material synthesis minimizes the issue of IrO_2 volatilization. Iridium loss has not been accounted for in calculation. As these materials are synthesized in relatively low temperatures, a small amount of porosity may be present in the materials. The synthesis temperature, however, could not be raised further to avoid any serious loss of Ir. All the materials are prepared in identical conditions which would give similar material quality in terms of Ir/Fe content, stoichiometry, as well as porosity. Furthermore, these materials are highly insulating, therefore a small amount of porosity would not affect the overall conductivity severely. The chemical phase purity of the samples are primarily checked with powder x-ray diffraction (XRD) where the data have been collected using a Rigaku MiniFlex diffractometer equipped with Cu-K_α source. The XRD data have been analyzed with Rietveld refinement program (FullProf software) [49].

To probe the charge state of constituent elements, x-ray photoemission spectroscopy (XPS) measurements have been done. The XPS measurements have been performed at base pressure of 10^{-11} mbar with an Omicron ultrahigh vacuum (UHV) chamber equipped with a nonmonochromatic Mg-K_α x-ray source ($h\nu = 1253.6$ eV) and a multichanneltron hemispherical electron energy analyzer (EA 125). The XPS data have been analyzed using XPS peak-fit 4.1 software. DC magnetization data are collected using the physical property measurement system (Quantum Design). The temperature dependent magnetization data have been collected in sweep mode with a temperature sweeping rate 1.5 K/min. Neutron powder diffraction (NPD) patterns over a wide angular range (3°–140°) are recorded at room temperature (counting time ∼6 h) using the powder diffractometer PD-2 ($\lambda = 1.2443$ Å) at Dhruva reactor, Trombay, India. Additional neutron diffraction patterns have been recorded at 5 and 150 K (counting time ∼30 h per temperature), to measure the magnetic Bragg peaks using the limited angular-range powder diffractometer PD-1 ($\lambda = 1.094$ Å) at Dhruva reactor, Trombay, India. For the NPD measurements, powder samples (∼4 g) are filled in a vanadium can of diameter around 6 mm where the low temperature measurements have been done using a closed cycle refrigerator (CCR). The neutron flux during these experiments was ∼5 × 10^5 neutrons/cm² s⁻¹. The NPD patterns are analyzed by Rietveld refinement program [49]. Temperature dependent electrical conductivity data are collected in a CCR based home-made insert and the magnetic field dependent electrical conductivity have been measured in an insert attached to a 9 T magnet (Nanomagnetics). The conductivity has been measured using the standard four-probe method with sintered pressed pellets for all the compositions. The data are collected in a sweep mode with temperature sweeping rate around 1.5 K/min.

III. COMPUTATIONAL DETAILS

Density functional theory (DFT) based electronic structure calculations are performed using the plane-wave basis set with
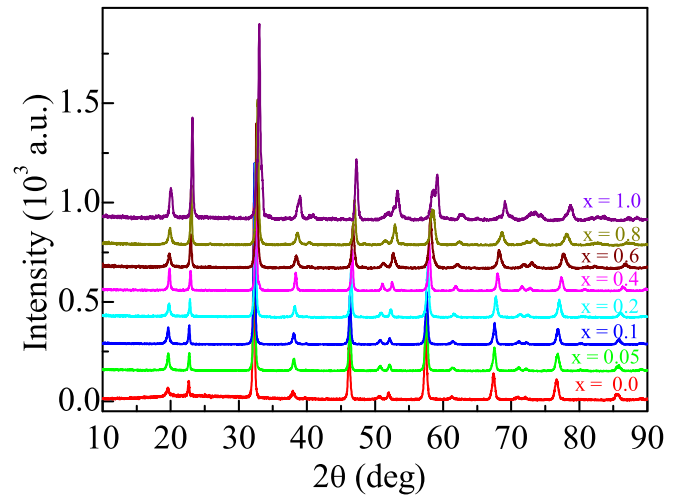

FIG. 1. XRD data collected at room temperature are shown for $(Sr_{1-x}Ca_x)_2FeIrO_6$ series with $x = 0.0, 0.05, 0.1, 0.2, 0.4, 0.6, 0.8, 1.0$.

a pseudopotential framework as incorporated in the Vienna *ab initio* simulation package (VASP) [50]. The generalized gradient exchange-correlation approximated (GGA) functional was employed following the Perdew-Burke-Ernzerhof (PBE) prescription [51]. The missing on-site electron-electron Coulomb correlations are taken through the inclusion Hubbard (U) in GGA + U [52,53]. The spin-orbit coupling (SOC) is introduced as a scalar relativistic correction to the original Hamiltonian. The plane-wave cutoff is employed to be 500 eV. A k-point mesh of 8 × 8 × 6 in the Brillouin zone (BZ) has been used for self-consistent calculations. The coordinates of the atomic positions are relaxed toward equilibrium until the Hellmann-Feynman force becomes less than 0.001 eV/Å, keeping the lattice parameters fixed at the experimentally determined values.

IV. RESULTS AND DISCUSSION

A. Structural analysis using x-ray diffraction

Figure 1 shows the XRD patterns for $(Sr_{1-x}Ca_x)_2FeIrO_6$ series at room temperature. As evident in Fig. 1, the symmetry in the structural data is retained over the series. However, with progressive substitution of Ca, the major observations are intensity of the peak at $2\theta = 23.2°$ increases, a small splitting arises in the peak situated at $2\theta = 59.1°$, and the position of peaks shifts to a higher 2θ value. Given that the ionic radii of Ca^{2+} (1.34 Å) and Sr^{2+} (1.44 Å) has some differences, even if a structural phase transition does not occur, a structural modification/distortion at local level is expected with the substitution of Ca for Sr.

A representative XRD pattern along with Rietveld refinement have been shown for two end members, i.e., $x = 0.0$ and 1.0 of the present series in Fig. 2. The crystal structure of Sr_2FeIrO_6 ($x = 0.0$) has already been reported by several groups including us. All the reports show a distorted structure but debate is between monoclinic and triclinic structure. For instance, Battle *et al.* [42] has shown a monoclinic-$P2_1/n$ structure from XRD data but their high-resolution
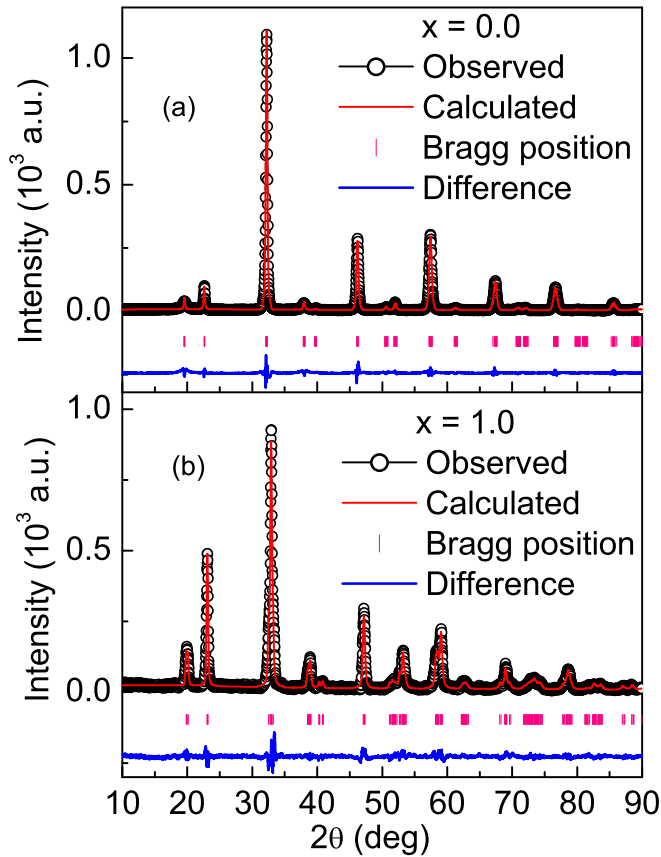
FIG. 2. (a) The Rietveld refinement of powder x-ray diffraction data with triclinic-$I\bar{1}$ symmetry for $x = 0.0$ compound in $(Sr_{1-x}Ca_x)_2FeIrO_6$ series. The experimentally observed intensity (open circle), calculated intensity (red line), and their difference (blue line) are shown in the figure. (b) The same for $x = 1.0$ compound of the present series.

FIG. 3. Lattice parameters (a) a, (b) b, (c) c, (d) α, (e) β, and (f) γ are plotted as a function of doping concentration x for $(Sr_{1-x}Ca_x)_2FeIrO_6$ series. Lines are a guide to the eyes.

neutron powder diffraction data indicate a triclinic-$I\bar{1}$ structure. Similarly, other groups have shown monoclinic-$P2_1/n$ or monoclinic-$I2/m$ structure using laboratory XRD, synchrotron XRD, and powder neutron diffraction data [43,44]. We have tried Rietveld refinement with all the above mentioned crystal structures for room temperature XRD data but out results show best fitting for triclinic-$I\bar{1}$ crystal structure as gauged by the lowest χ^2 value. For example, we obtain χ^2 values for triclinic-$I\bar{1}$, monoclinic-$P2_1/n$, or monoclinic-$I2/m$ structures of 4.78, 5.28, and 5.17, respectively [29]. We also obtain a similar lowest χ^2 value for triclinic-$I\bar{1}$ structure in Rietveld analysis with neutron powder diffraction data (discussed later). We have further verified, by DFT total energy calculations, taking into account both electron correlation and SOC effect for both triclinic and monoclinic symmetry. The results indicate that although the energetics are very similar, however, the triclinic symmetry structure is energetically lower than the monoclinic symmetry structure by an amount of ~2 meV/f.u.

Figure 2 in the present paper shows reasonably good Rietveld fitting with triclinic structure. Furthermore, on close inspection, the XRD data in Figs. 1 and 2 show multiple peaks related to the distorted structure which is not very clear in the
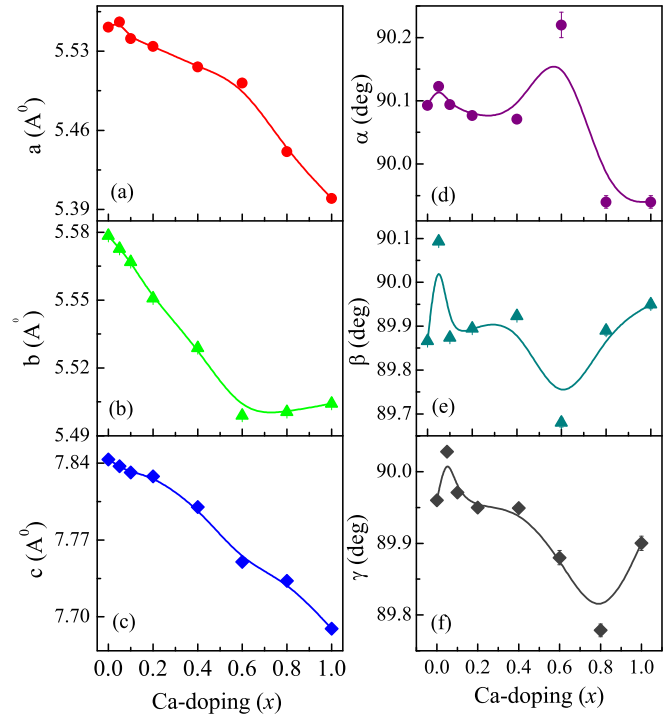
figures because XRD has a relatively low resolution. However, the neutron powder diffraction pattern in Fig. 9(a) indeed shows clear multiple peaks, and all the peaks are refined by Rietveld analysis with triclinic-$I\bar{1}$ structural symmetry. Here it can be mentioned that the results of all Rietveld analysis and energy calculations show a small difference between triclinic and monoclinic structure, but the triclinic structure consistently shows a stable structural phase for the present materials. Figure 2(a) displays the Rietveld refinement of XRD data with triclinic-$I\bar{1}$ symmetry for Sr_2FeIrO_6 ($x = 0.0$) sample, showing a reasonably good fitting. In fact, we find that the whole series in the present study can be fitted well with the same triclinic-$I\bar{1}$ crystal symmetry, as indicated by the lowest χ^2 value. Figure 2(b) shows the same Rietveld fitting for the Ca_2FeIrO_6 ($x = 1.0$) sample. The χ^2 values obtained from Rietveld refinement are 4.78, 2.62, 3.07, 2.20, 3.18, 2.03, 2.28, and 2.71 for $x = 0.0, 0.05, 0.1, 0.2, 0.4, 0.6, 0.8$, and 1.0 composition, respectively, which signifies a good fitting of XRD data. Here it can be mentioned that using the real structural parameters from XRD analysis, we calculate the tolerance factor (t) to be 0.95 and 0.77 for $x = 0.0$ and 1.0, respectively, which indicates a distorted crystal structure (monoclinic or triclinic) for these materials. A point to be noted here is that most of the Ir based double perovskites $(Sr, La)_2MIrO_6$ (M = Co, Mg, Zn, Cu, Ce) are reported to adopt distorted monoclinic or triclinic structure, as found in the literature [33,54–56].

The unit cell parameters (a, b, c, α, β, and γ), extracted from the refinement of XRD data, are shown in Fig. 3 as a function of doping concentration x. Although the triclinic-$I\bar{1}$ symmetry continues for the whole $(Sr_{1-x}Ca_x)_2FeIrO_6$ series,
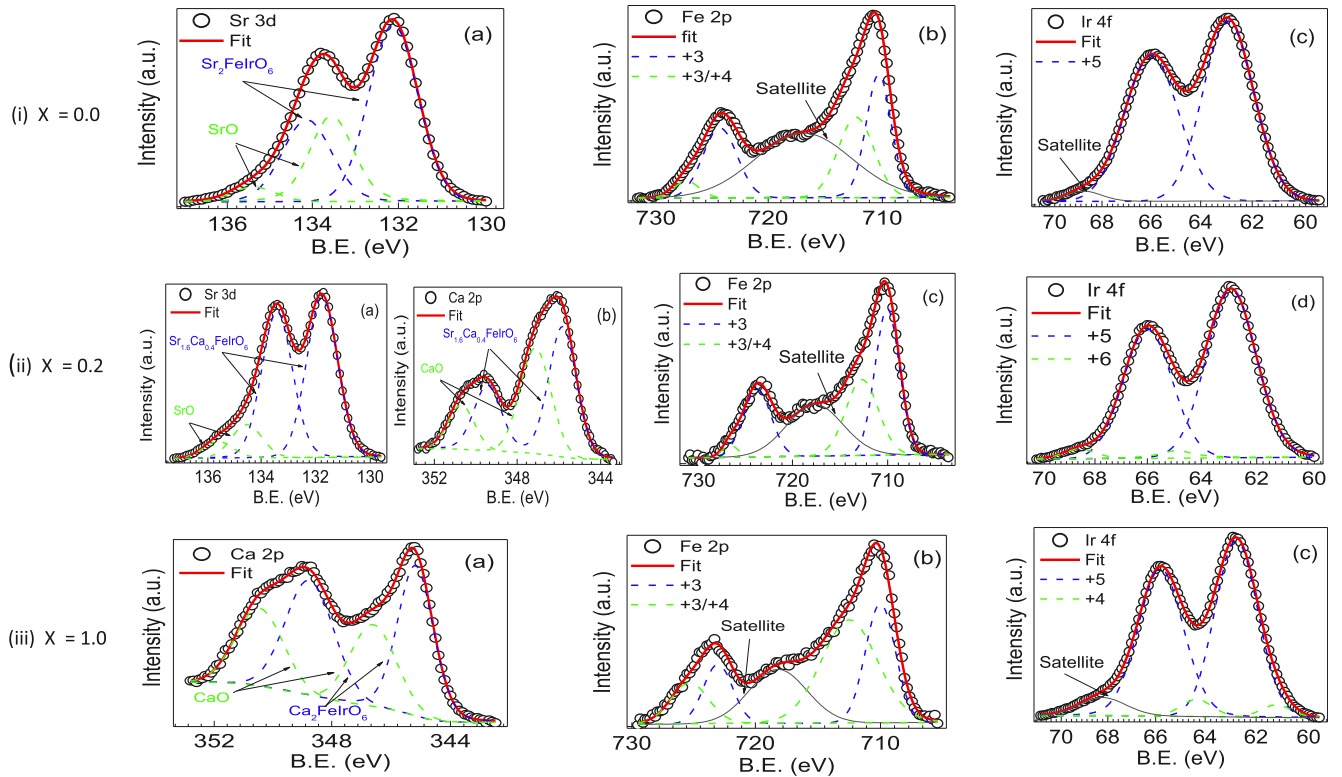
FIG. 4. The XPS spectrum are shown for two end members ($x = 0.0$ and 1.0) and an intermediate compound with $x = 0.2$ of $(Sr_{1-x}Ca_x)_2FeIrO_6$ series. Description of plots are (i) $x = 0.0$ [(a) Sr $3d$, (b) Fe $2p$, and (c) Ir $4f$], (ii) $x = 0.2$ [(a) Sr $3d$, (b) Ca $2p$, (c) Fe $2p$, and (d) Ir $4f$], and (iii) $x = 1.0$ [(a) Ca $2p$, (b) Fe $2p$, and (c) Ir $4f$]. Red and gray solid lines are due to fitting of the whole spectrum and satellite, respectively, whereas the individual fittings are shown in the dotted blue and green lines (see text).

the crystal structure becomes more distorted with doping. Lattice constants a, b, and c mostly decrease with doping. However, as seen in Fig. 3, all the structural parameters (a, b, c and angles α, β, and γ) show an anomalous variation around $x = 0.05$–0.1 and then 0.6. The decrease in lattice constants a, b, and c with doping concentration x is due to smaller ionic radii of Ca^{2+} compared to Sr^{2+}. Considering that this is an isoelectronic substitution, the doped Ca induces a chemical pressure at A site to modify the lattice parameters.

B. X-ray photoemission spectroscopy data

In order to understand the charge states of constituent transition metals, i.e., Fe/Ir and its effect on physical properties in $(Sr_{1-x}Ca_x)_2FeIrO_6$ series, the XPS measurements have been performed for doping concentrations $x = 0.0$, 0.2, and 1.0. The XPS data for representative $x = 0.0$, 0.2, and 1.0 are shown in Figs. 4(i), 4(ii), and 4(iii), respectively, as a function of binding energy (B.E.). The core levels have been fitted using Lorentzian components with a small admixture of Gaussian. Figures 4(i)(a) and 4(ii)(a) show Sr-$3d$ data for $x = 0.0$ and 0.2, respectively, where the spin-orbit split Sr-$3d_{5/2}$ and Sr-$3d_{3/2}$ peaks are seen at B.E. 132.1 and 133.9 eV, respectively (marked with a dotted blue line). In addition, our fitting indicates similar Sr-$3d_{5/2}$ and Sr-$3d_{3/2}$ contributions from SrO (green dotted line) while the red solid lines in figures indicate the total fitting of the data.

The XPS data of Ca-$2p$ are shown for $x = 0.2$ and 1.0 in Figs. 4(ii)(b) and 4(iii)(a), respectively. The similar spin-orbit split Ca-$2p_{3/2}$ and Ca-$2p_{1/2}$ peaks of DP ($Sr_{1.6}Ca_{0.4}FeIrO_6$, Ca_2FeIrO_6) and CaO are marked with dotted blue and green colors, respectively. The contribution from SrO/CaO in XPS spectra arises due to exposure of material surface to the atmosphere where oxidation of Sr/Ca takes place [57–59]. The analysis of Sr-$3d$ and Ca-$2p$ spectra indicates that Sr/Ca is in $2+$ charge state, as expected.

The XPS spectrum of Fe-$2p$ are shown in Figs. 4(i)(b), 4(ii)(c), and 4(iii)(b) for $x = 0.0$, 0.2, and 1.0, respectively. A pronounced satellite peak is seen in the figure at about 8 eV above the main peak. In XPS Fe-$2p$ spectrum, spin-orbit split $2p_{3/2}$ and $2p_{1/2}$ peaks are seen around 710 and 723.5 eV for Fe^{3+} and around 712 and 725.5 eV for Fe^{4+}, respectively. Moreover, a pronounced satellite peak on top of the shoulder is observed around 718 eV in case of Fe^{3+}, while a weak satellite feature is present in the case of Fe^{4+} [60–62]. In view of these, the Fe-$2p$ XPS spectra shown in Fig. 4 for the present materials suggest iron is in Fe^{3+} state. Individual peaks related to Fe-$2p_{3/2}$ and Fe-$2p_{1/2}$ states for Fe^{3+} charge state are marked in the dotted blue while the satellite peak is shown in gray. Using Mössbauer spectroscopy, Fe^{3+} ionic state has been evidenced in Sr_2FeIrO_6 [7]. Previous studies on iron based materials report multiple peaks corresponding to Fe^{3+} state where a satellite peak is seen exactly at 8 eV above the main peak [63–66]. The peaks shown with dotted green color in Fe-$2p$ spectra may be due to a Fe^{3+} complex, however, this also has been shown related to Fe^{4+} state [67].

Figures 4(i)(c), 4(ii)(d), and 4(iii)(c) show XPS data of Ir-$4f$ for $x = 0.0$, 0.2, and 1.0 material, respectively. The

Ir-$4f$ core level spectra are fitted well with two spin-orbit split peaks corresponding to Ir-$4f_{7/2}$ and Ir-$4f_{5/2}$ levels. In XPS Ir-$4f$ spectra, the spin-orbit split Ir-$4f_{7/2}$ and Ir-$4f_{5/2}$ doublets occur around 62 and 65 eV for Ir^{4+}, while for Ir^{5+} those peaks occur at little bit higher energies, between 63–64 and 66–68 eV, respectively [31,59,68–71]. For $x = 0.0$, these two peaks are observed at 62.9 and 65.9 eV with a satellite at 68.8 eV, where the difference between peaks is ~3 eV. These peak positions are consistent with Ir^{5+}. The $3 + /5+$ charge state of Fe/Ir as obtained from the analysis of XPS data for Sr_2FeIrO_6 are consistent with the charge state obtained from the analysis of our magnetization data as well as with the electronic structure calculations (discussed later). For $x = 0.2$, the peaks corresponding to Ir^{5+} are observed at 62.9 and 66.0 eV along with a weak contribution of Ir^{6+} state, seen at 64.9 and 68.6 eV. The peaks related to Ir^{5+} and Ir^{6+} are shown in dotted blue and green colors, respectively. Analysis of data reveals the content of Ir^{5+} and Ir^{6+} are about 95.1% and 4.9%, respectively. For $x = 1.0$ material, on the other hand, we find a small trace of Ir^{4+} along with Ir^{5+} and a gray colored satellite peak. The peak positions of Ir^{5+} are around 62.9 and 65.9 eV in the spectrum, whereas those of Ir^{+4} are found at 61.5 and 64.5 eV. The amount of Ir^{5+} and Ir^{4+} are analyzed to be around 94.1% and 5.9%, respectively. From the analysis of XPS data it is evident that iridium is mostly in Ir^{5+} charge state in the present series, while a small amount of neighboring charge states (i.e., Ir^{4+} and Ir^{6+}) are observed mostly due to nonstoichiometry in materials.

C. Magnetic study in $(Sr_{1-x}Ca_x)_2FeIrO_6$

Our previous study has shown that the Sr_2FeIrO_6 has prominent long-range AFM transition around 45 K, however, a close observation in magnetization data reveals a weak AFM transition at higher temperature around 120 K which is marked by an onset of bifurcation between zero field cooled (ZFC) and field cooled (FC) magnetization data [29]. Similar magnetic transition around 120 K, though with different features, has been reported for Sr_2FeIrO_6 in previous studies [42–44]. Furthermore, an analysis of magnetization data for Sr_2FeIrO_6 gives an effective magnetic moment (μ_{eff}) 6.19 μ_B/f.u. which closely matches with the calculated value 5.92 μ_B/f.u following the relation $\mu_{eff} = g\sqrt{S(S + 1)}$ where S is the total spin that indicates $3 + /5+$ charge state of Fe/Ir, respectively [29]. Our XPS data analysis in Fig. 4 regarding the charge states of transition metals are in fact consistent with the magnetization data for Sr_2FeIrO_6 [42–46].

The ZFC and FC magnetization data collected in the 1000 Oe magnetic field are shown in Figs. 5(a) and 5(b) for the present $(Sr_{1-x}Ca_x)_2FeIrO_6$ series. While the nature of bifurcation between ZFC and FC magnetization data as well as the magnetic transition at T_N changes with the Ca doping, the $M(T)$ shows a continuous decrease in high temperature PM state for all the samples. In the inset of Fig. 5(b), temperature derivative of magnetization data (dM/dT) are shown for $x = 0.0$ and 1.0 samples. As evident in the figure, the dM/dT indicates a dual magnetic transition for Sr_2FeIrO_6 around 45 and 120 K, while for Ca_2FeIrO_6 a single transition is observed around 75 K which is in agreement with a previous report [44]. Furthermore, the magnetic data show a
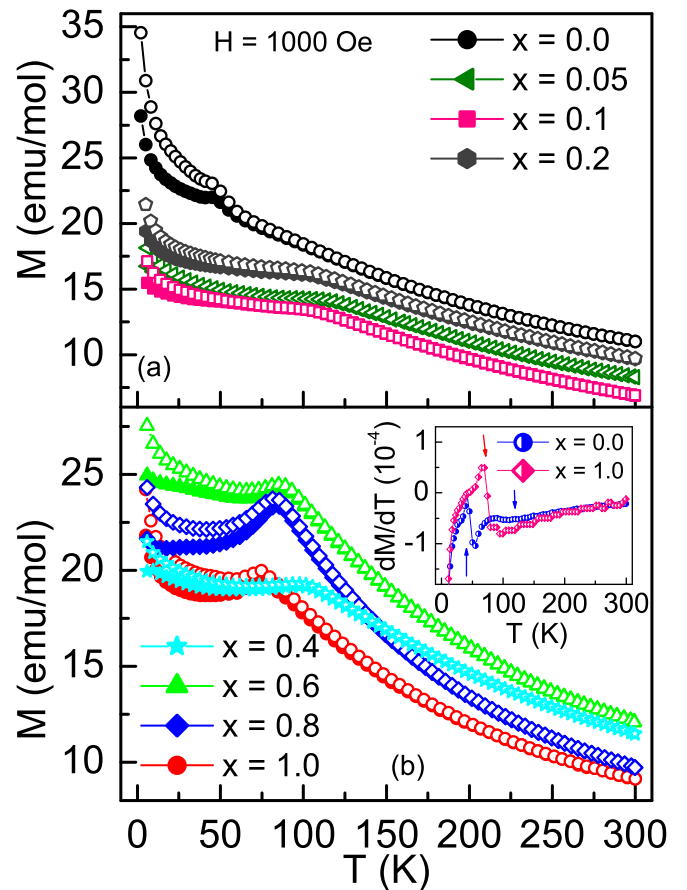

FIG. 5. DC magnetization data collected following ZFC and FC protocol at 1000 Oe magnetic field are shown as a function of temperature in (a) $x = 0.0, 0.05, 0.1, 0.2$ and (b) $x = 0.4, 0.6, 0.8, 1.0$ for $(Sr_{1-x}Ca_x)_2FeIrO_6$ series. The ZFC and FC data are represented by filled and open symbols, respectively. Inset of (b) shows the dM/dT plot for $x = 0.0$ and $x = 1.0$, where arrows indicate the transition temperatures of these materials.

relatively large moment in PM state and a small absolute value of dM/dT. While these could be due to an inhomogeneous magnetic state in PM state, the obtained moment agrees well with the previous reports of the same material [7], and also with other Ir based paramagnetic material $SrIrO_3$ single crystals [72]. The composition dependent transition temperature T_N is shown in Fig. 8(a) which shows T_N decreases almost monotonically with x. Note that unlike Sr_2FeIrO_6, we have observed only single transition in doped materials, at least it is not clearly evident in magnetization data. We further mention that other $3d$-$5d$ DP material, i.e., Sr_2FeOsO_6, shows two AFM phase transitions ($T_N \sim$ 140 and 67 K) with temperature where the magnetic phases differ by an alignment of spins structure in Fe-O layers [10,12,47]. In the present Sr_2FeIrO_6, the transition around 120 K is very weak, however, it needs a detailed investigation using microscopic experimental tools (neutron diffraction measurements discussed later). While previous studies report a single AFM transition (120 K) in Sr_2FeIrO_6, we show the possibility of double magnetic transition in this material [29]. It remains, however, interesting that with increasing structural distortion or x, the transition at low
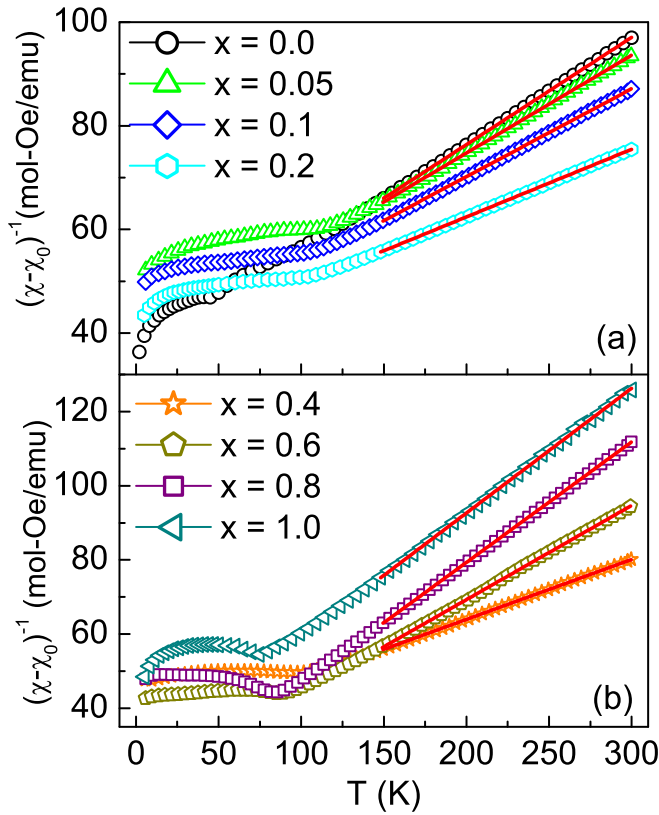
FIG. 6. A modified inverse magnetic susceptibility $(\chi-\chi_0)^{-1})$ deduced from ZFC magnetization data are shown as a function of temperature in (a) $x = 0.0, 0.05, 0.1, 0.2$ and (b) $x = 0.4, 0.6, 0.8, 1.0$ for $(Sr_{1-x}Ca_x)_2FeIrO_6$ series. Solid lines are due to the linear fit of the data using a modified Curie-Weiss model [Eq. (2)].
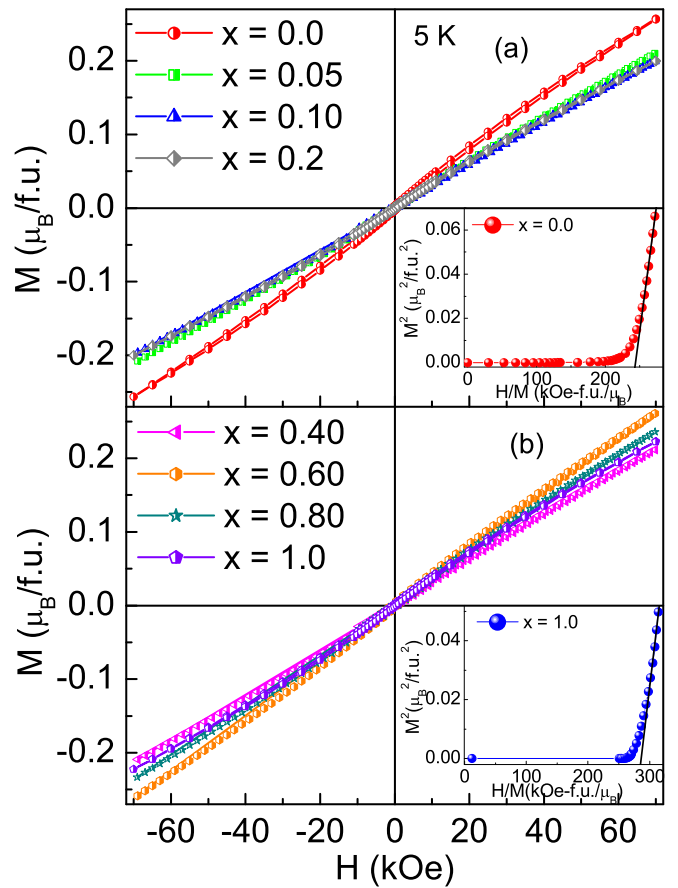

FIG. 7. Magnetic field dependent magnetization data $M(H)$ collected at 5 K are shown for (a) $x = 0.0, 0.05, 0.1, 0.2$ and (b) $x = 0.4, 0.6, 0.8, 1.0$ of $(Sr_{1-x}Ca_x)_2FeIrO_6$ series. Insets of (a) and (b) show the Arrott (M^2 vs H/M) plot for representative $x = 0.0$ and 1.0, respectively.

temperature is no more evident while the high temperature transition becomes prominent.

The magnetic susceptibility χ ($=M/H$) data in high temperature PM regime have been analyzed with modified Curie-Weiss (CW) behavior, Inverse magnetic susceptibility (χ^{-1}) data as a function of temperature for $x = 0.0, 0.05, 0.10, 0.20$ and $0.4, 0.6, 0.8, 1.0$ of $(Sr_{1-x}Ca_x)_2FeIrO_6$ series are shown in Figs. 6(a) and 6(b), respectively, where in the paramagnetic state χ^{-1} for all samples follows modified Curie-Weiss (CW) behavior. In the high temperature range data has been fitted well using the equation

$$\chi = \chi_0 + \frac{C}{T - \theta_P}, \tag{2}$$

where χ_0 is the temperature independent contribution to the susceptibility which originates from core diamagnetism or paramagnetic moment, C is the Curie constant, and θ_P is the CW temperature. The effective PM moment μ_{eff} has been calculated from C. The corrected inverse susceptibility $(\chi-\chi_0)^1$ as a function of temperature are shown in Figs. 6(a) and 6(b) for the present series where the straight line fitting in PM regime (150–300 K) demonstrates the CW behavior [Eq. (2)] in PM state. The parameters θ_P and μ_{eff} are shown in Figs. 8(b) and 8(c), respectively, as a function of doping concentration x (discussed later).

The magnetic field dependent isothermal magnetization $M(H)$ data collected at 5 K are shown in Figs. 7(a) and 7(b) for $x = 0.0, 0.05, 0.1, 0.2$ and $0.4, 0.6, 0.8, 1.0$, respectively, of $(Sr_{1-x}Ca_x)_2FeIrO_6$ series. For $x = 0.0$, the $M(H)$ data are almost linear till about 45 kOe, and above this field the $M(H)$ show a slight deviation from linearity with field. It is, however, evident in Fig. 7 that $M(H)$ data do not exhibit saturation for all the samples up to the maximum applied field, i.e., 70 kOe. This linearity in the $M(H)$ data indicates a dominant AFM-type interaction in these materials. We calculate the magnetic moment at 70 kOe (μ_H) to be 0.26 μ_B/f.u. for $x = 0.0$ which appears sufficiently small compared to its calculated value 5 μ_B/f.u. ($=gS\mu_B$, g is Landé g factor) taking contribution of Fe^{3+} ($S = 5/2$) and Ir^{5+} ($S = 0$). The experimentally determined μ_H has been shown in Fig. 8(e) with variation of x. The variation μ_H with x where it shows an initial dip at $x \sim 0.2$ is quite consistent with behavior of θ_P in Fig. 8(b). An increased value of $|\theta_P|$ promotes stronger AFM exchange across $x \sim 0.2$ which results in a reduced moment μ_H even in the presence of magnetic field.

Furthermore, a small hysteresis in the $M(H)$ data has been observed with coercive field $H_c \sim 590$ Oe and an remnant magnetization $M_r \sim 2.8 \times 10^{-3}$ μ_B/f.u for parent Sr_2FeIrO_6
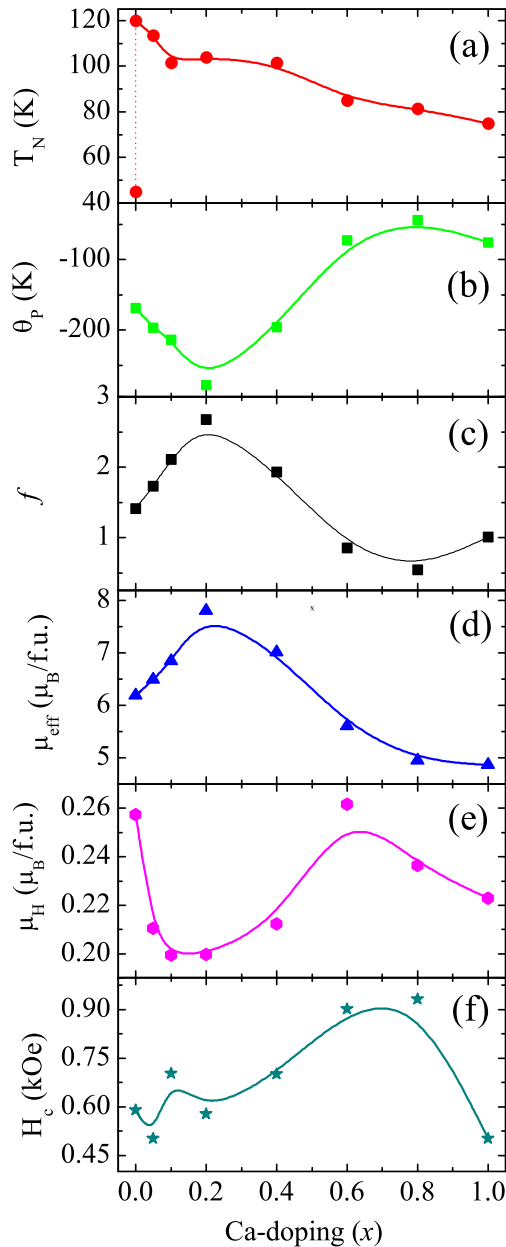
FIG. 8. (a) T_N, (b) θ_P, (c) frustration parameter f, (d) μ_{eff}, (e) μ_H, and (f) H_c are shown as a function of doping concentration x for $(\text{Sr}_{1-x}\text{Ca}_x)_2\text{FeIrO}_6$ series. Lines are a guide to the eyes.

($x = 0.0$) material. The respective H_c values for the present series are shown in Fig. 8(f). The H_c values, after showing a initial dip, maximizes for x in between 0.6 and 0.8. The remnant magnetization M_r also follows a similar trend where it first decreases from 2.8×10^{-3} to 2.1×10^{-3} μ_B/f.u for $x = 0.2$ and then increases to 3.75×10^{-3} μ_B/f.u for $x = 0.6$ and again decreases to 2.16×10^{-3} μ_B/f.u. This H_c and M_r rather follow the similar tend of θ_P with x. The nature of magnetism in these materials is further checked with Arrott's plot (M^2 vs H/M) [73], as shown in the insets of Figs. 7(a) and 7(b) for representative $x = 0.0$ and 1.0, respectively. A positive intercept due to linear fitting in high field regime of the Arrott plot signifies a FM nature of the system, whereas the negative intercept excludes the possibility of FM interactions.

Both insets of Fig. 7 indicate a negative intercept in the Arrott plot which implies a non-FM type exchange interaction in the present series in confirmation with the other results.

The magnetic parameters of the present series are noted in Fig. 8. The AFM transition temperature T_N shows almost a continuous decrease across the series [Fig. 8(a)], however, the low temperature AFM transition ($T_N \sim 45$ K) that is observed in $x = 0$ material, is not evident in Ca doped ones. However, the interesting effect of isoelectronic Ca substitution in the present series is observed in other magnetic parameters. For $\text{Sr}_2\text{FeIrO}_6$, the θ_P is found to be -169 K. While the sign θ_P is an indicative of non-FM or AFM type magnetic exchange interaction, its magnitude suggests the strength of interaction is reasonably strong. As evident in Fig. 8(b), while keeping the sign the same the magnitude of θ_P initially increases till around $x = 0.2$ reaching its value -278 K, and then it decreases. This initial increase of θ_P is quite interesting as T_N shows a continuous decrease. This implies the strength of AFM exchange interaction increases with an initial substitution of Ca till $x \sim 0.2$. Nonetheless, the higher magnitude of θ_P than the transition temperature T_N implies a magnetic frustration in the system. The calculated frustration parameter ($f = \theta_P/T_N$), which tentatively measures the level of frustration, has been shown in Fig. 8(c) for the present series. The $f > 1$ for parent $\text{Sr}_2\text{FeIrO}_6$ indicates a magnetic frustration is present in this material, which further increases till $x \sim$ 0.2 indicating frustration increases with initial substitution of Ca. The f, however, decreases for $x > 0.2$ while its value ~ 1 for $\text{Ca}_2\text{FeIrO}_6$ suggests an agreement between ordering temperature and strength of magnetic interaction. The double perovskites, indeed, have inherent geometrical frustration arising from its structural organization. As seen in the unit cell of $\text{Sr}_2\text{FeIrO}_6$ [Fig. 9(b)], Fe and Ir atoms occupy alternate positions. The Fe/Ir sublattices form different sets of tetrahedra where the vertices are occupied by Fe/Ir atoms. If the occupying elements are magnetic in nature and they are engaged in AFM type magnetic interactions, it generates magnetic frustration in the system. Here it can be mentioned that although present systems exhibit $f > 1$, its values are much lower than the value usually seen for frustrated systems ($f > 10$).

The effective magnetic moment μ_{eff}, on the other hand, shows an opposite behavior of θ_P, showing its maximum value for $x = 0.2$ material [Fig. 8(d)]. The μ_{eff} has been calculated theoretically using the formula ($\mu_{\text{eff}} = \sqrt{(\mu_{\text{Fe}})^2 + (\mu_{\text{Ir}})^2}$), where μ_{Fe} and μ_{Ir} are the magnetic moment of Fe^{+3} and Ir^{+5} cations, respectively. For $\text{Sr}_2\text{FeIrO}_6$, μ_{eff} is found to be close to a theoretically calculated value with Fe^{3+} and Ir^{5+} charge states, where Fe^{3+} ($S = 5/2$) only contributes to the moment while Ir^{5+} ($J_{\text{eff}} = 0$) is considered to be nonmagnetic. Under the picture of cubic crystal field and strong SOC, spins of Ir^{5+} ($5d^4$) completely occupy the $J_{\text{eff}} = 3/2$ state with zero effective magnetic moment. On the contrary, if one considers Fe^{3+} is in $S = 5/2$ high-spin state and Ir^{5+} is in $S = 1$ low-spin state under the strong distortion driven splitting, then in addition to spin moment there would be orbital contribution to the moment at the Ir site. Considering both orbital and spin magnetic moment of Fe and Ir, the total calculated moment comes out around 6.41 μ_B/f.u, which is quite close to the experimentally determined value of μ_{eff} [Fig. 8(d)]. Although
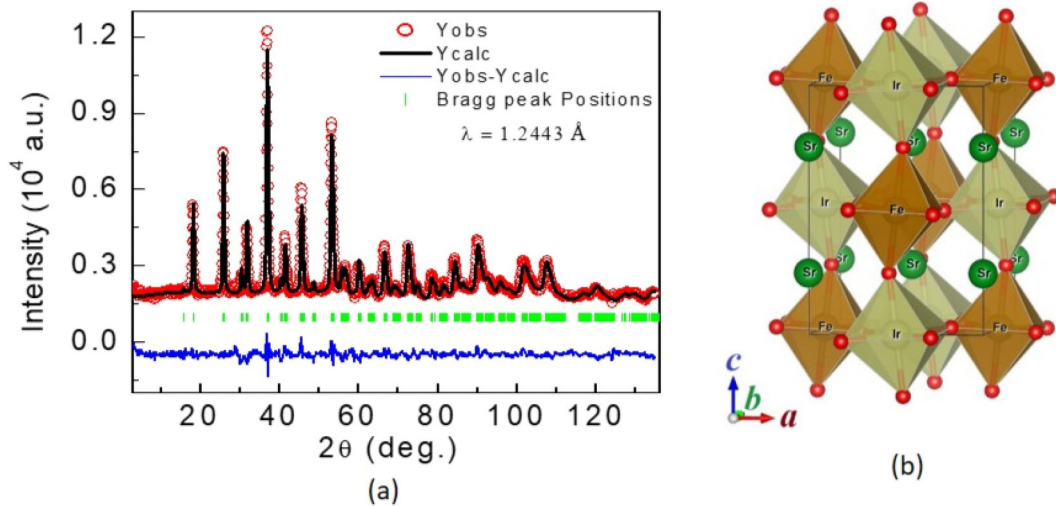
FIG. 9. The experimentally observed (circles) and calculated (solid lines through the data points) neutron diffraction patterns for Sr_2FeIrO_6 at room temperature measured by PD-2 ($\lambda = 1.2443$ Å). The solid lines at the bottom of the each panel represent the difference between observed and calculated patterns. The vertical bars indicate the positions of allowed nuclear Bragg peaks. (b) The crystal structure of Sr_2FeIrO_6.

the bulk magnetization measurements are not quite sensitive to the orbital moment part, if we consider only spin moment of Fe and Ir the ideal magnetic moment comes out to be $\sim 6.56\,\mu_B$, which is also close to the measured μ_{eff} values. Here the point to be noted is that spectroscopic studies do not find any evidences of charge state changes with Ca at Fe/Ir sites (Fig. 4). Moreover, $3d$-Fe^{3+} and $5d$-Ir^{5+} usually prefer to stay in high- and low-spin state, respectively, considering the six coordinated octahedral environment of inorganic ligand and resulting competition between the crystal field and the electron-electron Coulomb correlation. Therefore, we tried to understand the spin state through the electronic structure calculations presented afterwards. It is clearly understood that the substitution of isoelectronic Ca at Sr site will unlikely change the Fe/Ir charge state but would introduce a local distortion in respective Fe/Ir octahedra. This would influence the crystal field effect, hence the overall magnetic behavior. For instance, Cao *et al.* [35] have discussed the possibility of different magnetic states of Ir^{5+} ($S = 0$ and 1) in DP Sr_2YIrO_6 which mainly originates due to an interplay between SOC (noncubic) crystal fields and local magnetic exchange interactions. However, this noncubic crystal field varies from material to material based on their lattice distortion.

D. Neutron powder diffraction study on Sr_2FeIrO_6

To understand the crystal structure down to low temperature as well as to find out the magnetic structure in Sr_2FeIrO_6 ($x = 0$), neutron powder diffraction (NPD) measurements have been carried out at 300, 150, and 5 K, which represent both nonmagnetic and magnetic states. The crystal structure for Sr_2FeIrO_6 is found to be triclinic with space group $I\bar{1}$ over the studied temperature range 5–300 K and is consistent with the structure obtained from the XRD data (Fig. 2). In our Rietveld analysis we obtain lower χ^2 value with triclinic-$I\bar{1}$ symmetry (4.92) compared to monoclinic-$I2/m$ structure (5.26), however, the difference is not very significant. Nonetheless, the analysis indicates a distorted crystal

structure (triclinic/monoclinic) which is also consistent with multiple peaks in diffraction pattern [Fig. 9(a)]. The Rietveld refinement of neutron diffraction pattern at room temperature is shown in Fig. 9(a). The refined structural parameters are given in Table I. The schematic representation of the crystal structure of Sr_2FeIrO_6 is shown in Fig. 9(b). Our Rietveld analysis also indicates a relatively small antisite disorder of about 9(2)% among the Ir and Fe sites in the parent Sr_2FeIrO_6 compound. We hope that a similar trend of antisite disorder will be retained across the series. Given that the degree of antisite disorder depends on the difference between ionic radii and the charge state of involved transition metal cations, this has a large impact on the physical properties of materials, the estimated disorder in the present systems is comparable to $3d$-$5d$ based other double perovskite systems [54,74].

The neutron diffraction patterns measured at 5 (magnetically ordered state) and 150 K (paramagnetic state) are shown in Fig. 10(a). Appearance of additional weak magnetic Bragg peaks at $\sim 6.9°$ and $13.4°$ are evident in the diffraction pattern measured at 5 K, confirming an antiferromagnetic ordering in Sr_2FeIrO_6. These two magnetic Bragg peaks could be indexed with a propagation vector $k = (0, 0.5, 0.5)$ with respect to the triclinic nuclear unit cell. The symmetry-allowed magnetic structure is determined by a representation analysis using the program BASIREPS available within the FULLPROF suite [49]. The symmetry analysis reveals that there is only one possible magnetic structure. The two phase (nuclear + magnetic) refinement of the measured diffraction pattern at 5 K is shown in Fig. 9(c). A good agreement between observed and calculated patterns is evident ($R_{mag} \sim 17\%$). The corresponding magnetic structure is shown in the inset of Fig. 9(c) which is found to be pure antiferromagnetic in nature without having any net magnetization per unit cell. At 5 K, the site ordered moments of Fe and Ir ions are found to be $\sim 4.5(2)$ and $0.5(3)\,\mu_B$/site, respectively. The Fe and Ir moments are aligned along the c and a axes, respectively, i.e., the moments are orthogonal to each other. The derive magnetic ground state is in agreement with the same obtained by DFT calculation

TABLE I. The Rietveld refined lattice constant (a, b, c), fractional atomic coordinates, and isotropic thermal parameters (B_{iso}) for Sr_2FeIrO_6 at 300 K.

300 K			
Space group $= I\bar{1}$,	$a = 5.558(1)$ Å,	$b = 5.569(1)$ Å,	$c = 7.8082(6)$ Å,
$\alpha = 90.30(1)°$	$\beta = 89.37(1)°$	$\gamma = 89.92(1)°$	$V = 241.72(6)$ Å^3
Atom	x/a	y/b	z/c
Sr	0.5009	0.4975	0.2520
Fe	0.0	0.5	0.0
Ir	0.5	0.0	0.0
O1	0.2520	0.2612	−0.0038
O2	0.2245	0.7799	−0.0162
O3	0.4554	0.0094	0.2479

(discussed later). The obtained magnetic structure is further in good agreement with that, as reported by Kayser *et al.* [45].

E. Electronic transport in $(Sr_{1-x}Ca_x)_2FeIrO_6$

The electrical resistivity (ρ) as a function of temperature are shown in Fig. 11 for $(Sr_{1-x}Ca_x)_2FeIrO_6$ series. From the figure it is evident that the resistivity increases sharply with decrease in temperature. At very low temperature the resistivity increases by several orders of magnitude than its room temperature value. Moreover, an insulating nature of charge transport is apparent throughout the temperature range for the whole series. For $x = 0.0$ we observe a change in slope of $\rho(T)$ data across its low temperature magnetic transition around 45 K [29]. The evolution of resistivity with composition in the present series is though nonmonotonic. The left inset of Fig. 11 shows the resistivity value at 40 K for varying Ca composition. As seen in the figure, the resistivity initially shows a peak at $x \sim 0.1$ and then its value increases by several

orders and shows another peak at $x \sim 0.6$. This nonmonotonic variation of $\rho(x)$ mimics that of structural parameters which also show an anomalous change across $x = 0.1$ and 0.6 (Fig. 3). Therefore, Figs. 3, 8, and 11 together suggest that the evolution of structural, magnetic, and electrical transport behavior in the present series are correlated.

This series of samples show a highly insulating state where the effect of magnetic field on charge transport has been checked at low temperature. The right inset of Fig. 11 shows the magnetoresistance (MR), expressed as $[\Delta\rho/\rho_0(\%) = (\rho - \rho_0)/\rho_0 \times 100]$ for $x = 1.0$ at 25 K. A negative MR has been observed till the maximum applied field of 30 kOe. The observed MR is almost linear and shows a little change (-3%) with field. Usually the materials with sizable SOC effect display positive MR induced by weak antilocalization (WAL) effect. The prominent examples are Bi_2Se_3 [75], Bi_2Ti_3 [76], and even in iridate Na_2IrO_3 films [77]. However, the negative MR at low temperatures is mainly
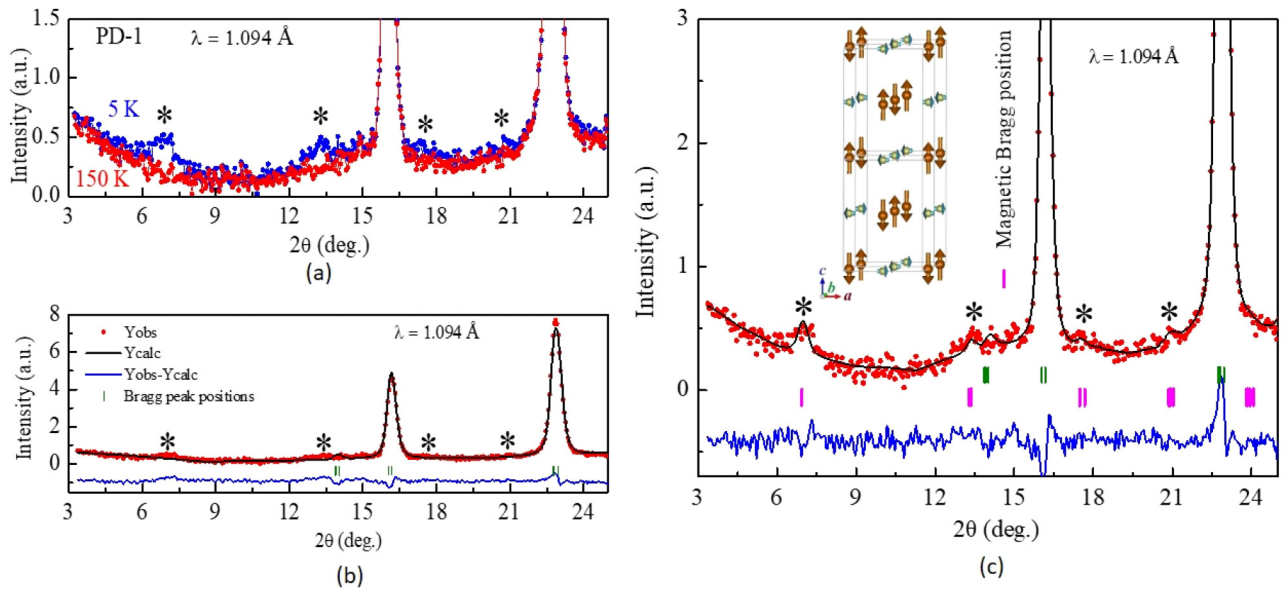

FIG. 10. The neutron diffraction patterns for Sr_2FeIrO_6 measured at 5 and 150 K by PD-1 ($\lambda = 1.094$ Å). The patterns are zoomed over the lower angular range to show the magnetic Bragg peaks. The magnetic peaks at 5 K are marked by asterisks. (b) The Rietveld refined (considering only the nuclear phase) neutron diffraction pattern measured at 5 K. (c) The Rietveld refined (considering nuclear and magnetic phases) neutron diffraction pattern measured at 5 K. The vertical bars indicate the positions of allowed nuclear (top panel) and magnetic (bottom panel) Bragg peaks. The inset shows the derived magnetic structure for Sr_2FeIrO_6.

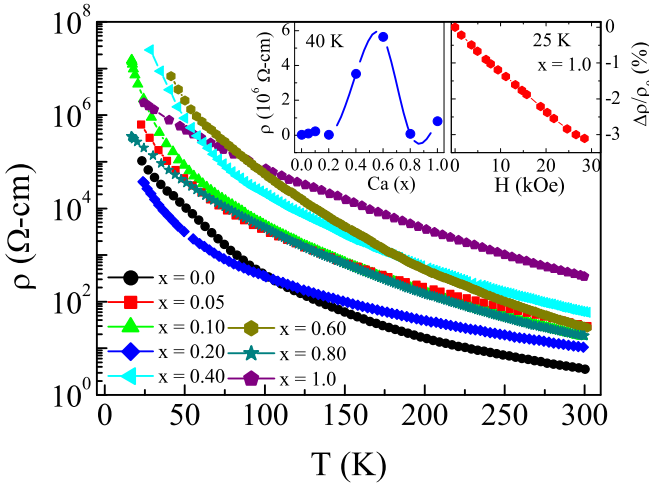FIG. 11. Resistivity data as a function of temperature are shown in semi-log scale for $(Sr_{1-x}Ca_x)_2FeIrO_6$ series. Left inset shows the resistivity value at 40 K against Ca doping showing a peak around $x = 0.1$ and 0.6. The line is a guide to the eyes. Right inset shows the MR data collected at 25 K for $x = 1.0$ material till 30 kOe.

understood in terms of weak localization (WL) effect, hopping conduction, and related magnetic scattering effect. This is related to the quantum interference (QI) effect which is largely viewed as the quantum correction in the classical Drude model for electronic conduction. In the case of hopping mediated conduction, the probability of hopping between two occurring sites depends on an interference of connecting paths. The effect of magnetic field leads to a destruction of QI effect producing a negative MR. Following an approach of averaging the logarithm of conductivity over many random paths, it has been shown that the effect of magnetic field is linear over charge conduction, showing a linear negative MR [78].

In our previous study we have shown that the electron conduction in Sr_2FeIrO_6 DP follows Mott's three-dimensional (3D) variable range hopping (VRH) model. With the substitution of Ca at Sr site, we do not find any change in the electron conduction behavior. The electron conduction mechanism over the series can be described well with the 3D VRH model [79]

$$\rho = \rho_0 \exp\left[\left(\frac{T_0}{T}\right)^4\right], \tag{3}$$

where T_0 is the characteristics temperature which is given as

$$T_0 = \frac{18}{k_B N(E_F)\xi^3}, \tag{4}$$

where k_B is the Boltzmann constant and $N(E_F)$ and ξ are the density of states (DOS) at the Fermi surface and localization length, respectively. Figures 12(a) and 12(b) show $\log(\rho)$ vs $T^{-1/4}$ plot of the $\rho(T)$ data following Eq. (3) for $x = 0.0$, 0.05, 0.1, 0.2 and 0.4, 0.6, 0.8, 1.0 of $(Sr_{1-x}Ca_x)_2FeIrO_6$ series, respectively. We have previously shown that the $\rho(T)$ of Sr_2FeIrO_6 can be fitted in two different temperature ranges with a crossover around 45 K (T_N). Given that $N(E_F)$ does not change appreciably over temperature in insulators, this change in slope (T_0) across the magnetic transition temperature can be through change in localization length [Eq. (4)]. As evident in
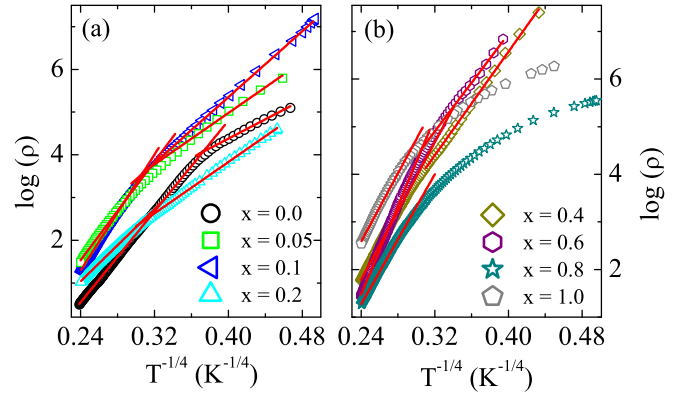

FIG. 12. $\log(\rho)$ vs $T^{-1/4}$ plot of resistivity data following Eq. (3) of VRH model are shown for (a) $x = 0.0$, 0.05, 0.1, 0.2 and (b) $x = 0.4$, 0.6, 0.8, 1.0 of $(Sr_{1-x}Ca_x)_2FeIrO_6$ series. Red solid line is due to the fit of the resistivity data.

Fig. 12, the $\rho(T)$ can be fitted with Eq. (3) in two different linear regimes till $x = 0.6$, however, in $x = 0.8$ and 1.0 materials Eq. (3) is obeyed only in a high temperature regime. Different regions in the fitting of $\rho(T)$ data closely follow the magnetic transitions in these materials. The temperature range and the characteristics temperature T_0 obtained from the fitting of the resistivity data are shown in Table II.

As evident in Table II, the change of T_0 parameter with composition is nonmonotonic. Furthermore, the change in T_0 with temperature for a specific material is likely due to an increase or decrease in the localization length ξ since the $N(E_F)$ would not change significantly in the case of insulators. Nonetheless, as the resistivity, crystal structure, and magnetism exhibit large change with doping concentration x, therefore we believe that both $N(E_F)$ and ξ contribute for the modification of T_0.

TABLE II. Temperature range and characteristics temperature (T_0) obtained using Eq. (4) from the fitting of resistivity data are shown with doping concentration (x) for $(Sr_{1-x}Ca_x)_2FeIrO_6$ series.

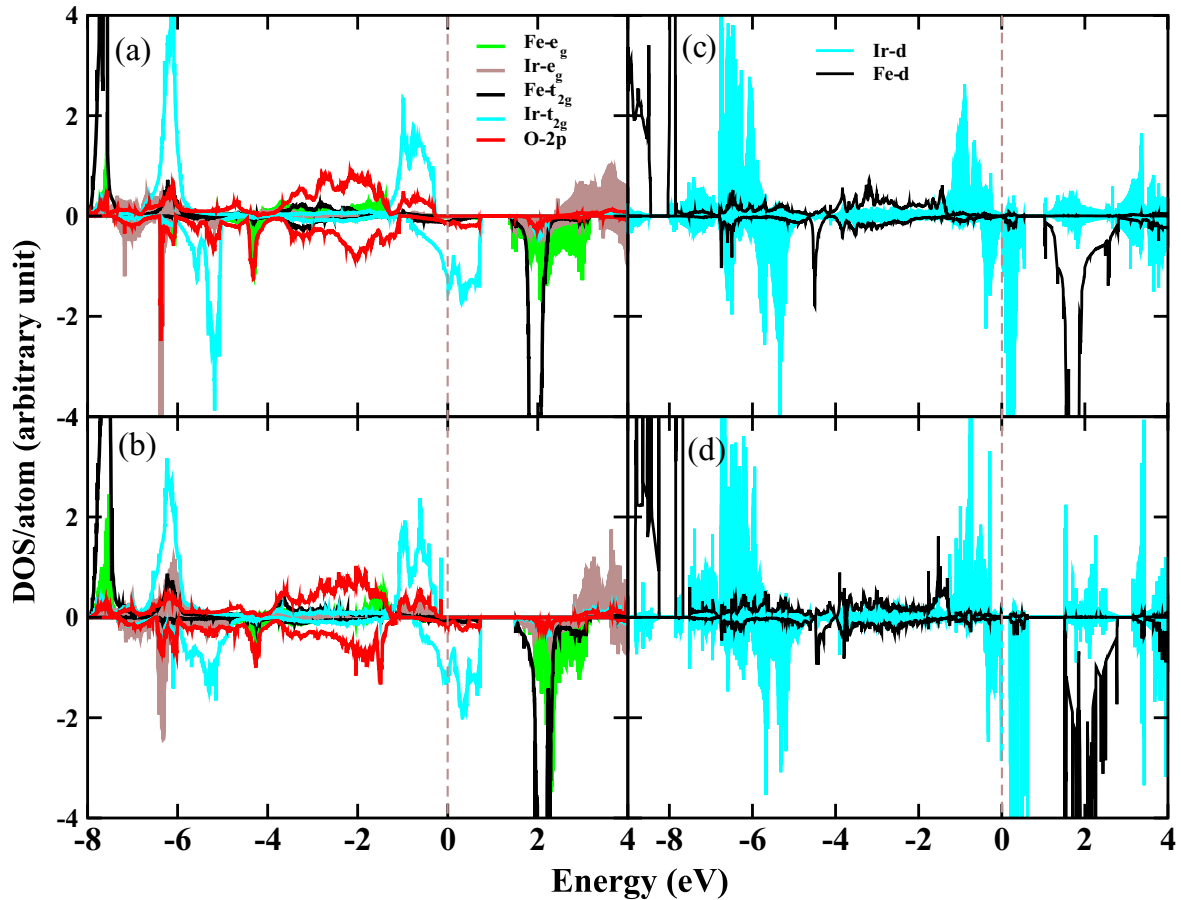| Sample (x)	Temperature range (K)	T_0 (10^5 K)
0.0	300–52	0.16
	45–20	4.93
0.05	300–125	6.9
	60–22	0.51
0.10	300–95	13.3
	83–20	1.38
0.2	300–95	2.0
	84–24	0.51
0.4	300–122	17.02
	82–28	5.46
0.6	300–122	46.43
	72–41	4.27
0.8	300–140	13.6
	122–65	1.51
	35–16	0.18
1.0	300–110	16.57
	105–66	9.4
	65–24	0.63

FIG. 13. The calculated GGA $+ U$ orbital projected DOS for the FM state are shown for (a) Sr_2FeIrO_6 and (b) Ca_2FeIrO_6. The (c) and (d) show the similar GGA $+ U$ DOS calculated for the energetically lowest AFM state for Sr_2FeIrO_6 and Ca_2FeIrO_6, respectively. The used U values are $U_{eff}^{Fe} = 5$ eV and $U_{eff}^{Ir} = 2$ eV. The Fermi energy is set at zero in the energy scale.

F. Electronic structure calculations

To understand the observed experimental results in the present series of materials from a microscopic point of view, we have done the electronic structure calculations at the DFT level, by taking care of electronic correlation (GGG $+ U$) through Hubbard U needed for transition metals as well as by considering spin-orbit coupling (GGG $+ U +$ SOC) required for the $5d$ elements. We have done calculations with different spin configurations. The calculated electronic density of states (DOS) through GGA $+ U$ formalism for both ferromagnetic (FM) and antiferromagnetic (AFM) spin alignments are shown in Fig. 13. For all the calculations we have used $U_{eff}^{Fe} = 5$ eV and $U_{eff}^{Ir} = 2$ eV, where $U_{eff} = U - J_H$ (J_H is the Hund's coupling, set to be 0.9 eV) which suits well according to $3d$ and $5d$ elements. The GGA $+ U$ calculated DOS for the FM spin alignments turn out to be half-metallic in nature with a finite DOS at the Fermi level in the minority spin channel coming from the Ir-t_{2g} states, while the majority spin channel shows a gap for the both Sr_2FeIrO_6 (SFIO) and Ca_2FeIrO_6 (CFIO), as shown in the Figs. 13(a) and 13(b), respectively.

Interestingly, the calculated GGA $+ U$ DOS with exactly the same values of Hubbard U (mentioned earlier), but with the AFM spin configuration instead of FM configuration, is able to open a gap in both spin channels by splitting the minority Ir-t_{2g} bands for both SFIO and CFIO, as shown in Figs. 13(c) and 13(d), respectively. Although the gaps at the Fermi level are very tiny (0.02 eV for SFIO and 0.2 eV for CFIO), however, only decent Hubbard U along with AFM spin correlation is able to open a gap in electronic band structure over the entire Brillouin zone, resulting in an insulating state for the both SFIO and CFIO. Given that the present $(Sr_{1-x}Ca_x)_2FeIrO_6$ series exhibits an insulating and AFM ground state (see Figs. 5, 7, and 11), our calculations indeed agree with the experimental evidences and indicate that the investigated materials falls under the category of weak Mott-type AFM insulator, as the electronic correlations for the $5d$-Ir is comparatively weaker. Also, we understand that the enhanced gap at the Fermi level in CFIO compared to the SFIO in the GGA $+ U$ calculations with an AFM state [Figs. 13(c) and 13(d)] is due to an enhanced structural distortion in CFIO compared to that in SFIO. The point to be further noted is that a gapped insulating ground state can also be realized even with FM correlation for an unphysical high value of Hubbard U at the $5d$-Ir elements (i.e., $U_{eff}^{Ir} \geqslant 4$ eV), which is due to the splitting of Ir-t_{2g} manifold into lower and upper Hubbard-like bands, very similar to that of the typical correlation driven Mott-insulator cases.

The closure investigation of the orbital projected DOS, as shown in Figs. 13(a) and 13(b), reveal that due to the distorted octahedral environment, the Fe-d states are broadly split into t_{2g}-e_g states, where both of the states are completely filled in the majority spin channel and completely empty in the minority spin channel, for both SFIO and CFIO. Similarly, the Ir-d states are split into low lying t_{2g} and high lying e_g states, however, the Ir-t_{2g} states are completely filled in the majority spin channel and partially filled in the minority spin channel having dominant contribution near the Fermi level. The Ir-e_g states, on the other hand, are completely empty in both spin channels lying 3 to 4 eV above the Fermi level in the conduction band. The calculated magnetic moment (Fe = 4.28 μ_B/site and Ir = 1.07 μ_B/site) and DOS suggest that iron is in Fe^{3+} ($3d^5$) nominal valence state, whereas iridium is in Ir^{5+} ($5d^4$) nominal valence state with high spin ($S = 5/2$) and low spin ($S = 1$) state for Fe and Ir, respectively, for both SFIO and CFIO. The calculated magnetic moments and the valence states support the experimental results, as seen in the XPS and neutron measurements. The substantial hybridization between Fe/Ir-d and O-2p states are evident from the DOS as well as from induced magnetic moment at oxygen sites (average moment 0.06 μ_B/site). The reduced moment at the Ir sites compared to that of the ideal value are due to the substantial orbital contribution and hybridization effect which will be discussed in the next section.

To understand the influence of spin-orbit coupling (SOC), the electronic band structure of SFIO and CFIO have been calculated taking combination of GGA + U + AFM + SOC along the high symmetry direction of the Brillouin zone (BZ) after fixing the spin quantization axis along [001] (Fig. 14). Due to the introduction of SOC, the degeneracy of the bands is broken, however, there are no such drastic differences between SFIO and CFIO band structures. As evident from the band structure in Fig. 14, there is an indirect band gap between Γ and M point in the BZ, which is slightly higher in CFIO than that in SFIO due to increased structural distortion caused by the smaller cationic size of Ca. Although the gap for both compounds has been enhanced due to the inclusion of SOC, compared to the the GGA + U calculations, however, the enhancement is more prominent in the case of SFIO than the CFIO, as the structural distortion is larger for the CFIO compared to that of the SFIO, which competes with the strength of the SOC. Also, there are no such drastic changes found in the band structure between GGA + U and GGA + U + SOC calculations, except the lifting of band degeneracy at a few selected K points and the enhancement of the band gap. The calculations show that the Fe spin magnetic moment minimally changes after the inclusion of SOC for both SFIO and CFIO, with a small orbital magnetic moment emerging which is expected due to the quenching of orbital degrees of freedom in d^5 high spin configuration. On the other side, the Ir spin magnetic moment [Ir-SFIO = 0.62 μ_B/site, Ir-CFIO = 0.61 μ_B/site] reduces substantially due to introduction of SOC. In addition to that, a large orbital magnetic moment around 0.25 μ_B/site with the same sign as that of the spin moment has been found for both SFIO and CFIO. The point to be noted here is that, although there are substantial orbital magnetic moments emerge at Ir site, still the orbital magnetic moment is smaller than the corresponding
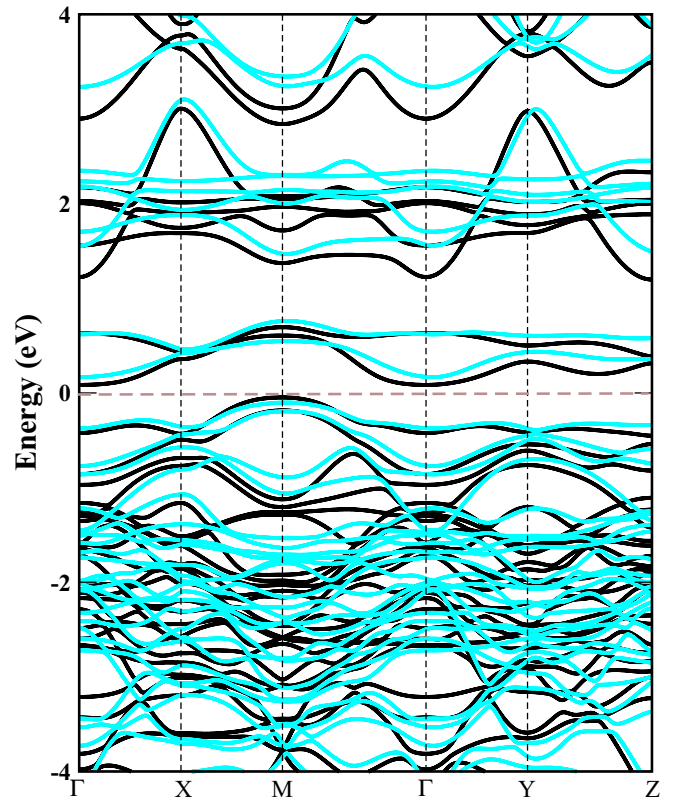

FIG. 14. The calculated GGA + U + SOC electronic band structure of AFM state are shown for SFIO (black) and CFIO (cyan). The Fermi energy is set at zero in the energy scale.

spin moment ($\mu^{orb}/\mu^{spin} \approx 0.5$). This suggests that for present materials, the effective strength of the SOC is small compared to that of the conventional strong SOC-driven Mott insulators such as Sr_2IrO_4, $A_2Ir_2O_7$, and Na_2IrO_3 [25–28,80,81], where the ratio (μ^{orb}/μ^{spin}) is close to as high as 2. Besides that, our calculations indicate even though SOC is required to stabilize an AFM state and enhance the band gap value, SOC is not essentially required to open a gap in the DOS or to induce an insulating state in present materials. This suggests these materials neither belong to the conventional correlation-driven Mott insulators nor the conventional SOC-driven Mott insulator (J_{eff} states), rather they can be classified as the "SOC enhanced correlation-driven AFM-Mott insulator."

We have examined the stability of magnetic ground state (FM or AFM) from the total energy perspective and have found that SOC is indeed needed to stabilize the AFM ground state over the FM ordering for both SFIO and CFIO by an amount of 2.35 and 25.56 meV/f.u., respectively. We have also investigated the energetics of different AFM spin configurations and the calculations show that in-plane (ab plane) nearest neighbor Fe and Ir spins are coupled antiferromagnetically, whereas out-of-plane (c direction) nearest neighbor Fe and Ir spins are coupled ferromagnetically, which is consistent with the neutron diffraction measurements as shown in the inset of Fig. 10(c). However, the interpenetrating two fcc lattices of Fe and Ir form a frustrated lattice where all the nearest neighbor interactions are not simultaneously satisfied, as evident from both theoretical calculations as well as experimental

results obtained from neutron diffraction. From the energy differences, it is clear that the magnetic exchange interactions between Fe and Ir sites are almost an order of magnitude stronger in the case of CFIO than that of the SFIO. In ordered DPs, the superexchange interactions are mainly dominated via two pathways; one through nearest neighbor (NN) Fe-O-Ir and another through next nearest neighbors (NNN), i.e., Fe-O-Ir-O-Fe and/or Ir-O-Fe-O-Ir pathways, as governed by the Goodenough-Kanamori angular rule [82,83]. However, as the size of A-site cation controls the superexchange angle, the strength and sign of the exchange interactions are tuned accordingly. With Ca doping, our calculations indeed indicate that the superexchange angles are changed substantially. For instance, in CFIO ($\sim 150°$) the angles are more deviated from the ideal $180°$, compared to SFIO ($\sim 166°$). For intermediate doping levels, the evolution of angles is nonmonotonic due to an uneven distortion in the local environment. The electronic structure total energy calculations clearly indicate that the AFM exchange interactions between different magnetic sites in CFIO is much stronger than that of the SFIO. These theoretical results are also in agreement with the experimentally determined ordering temperature T_N of present series (Fig. 7).

Since the two end compounds, i.e., SFIO ($x = 0$) and CFIO ($x = 1$) in present $(Sr_{1-x}Ca_x)_2FeIrO_6$ series show many similarities as well as dissimilarities, it would be interesting to explore the evolution of electronic structure across the series at microscopic level. Therefore, we have started with $\sqrt{2} \times \sqrt{2} \times 1$ supercell of SFIO that contains eight Sr sites and four Fe and Ir sites, each with a total of 40 atoms in the supercell. We have performed Ca-doping calculations for specific doping levels, viz. 12.5%, 25%, 37.5%, and 62.5%, due to constraint of the size of the supercell. The calculated GGA + U + SOC (spin quantization axis 001) DOS in AFM ground state are shown in Fig. 15. The electronic structure of the doped systems are not drastically different than the two end compounds, i.e., SFIO and CFIO. Figure 15 clearly indicates that near Fermi energy the Ir-5d states dominate similar to SFIO and CFIO. Also, as Ca doping concentration increases, the Ir-t_{2g} conduction bands are pushed up and the band gap increases which attains maximum value for the optimal level at $x = 0.375$ doping. In addition, the bandwidth of the valence band shirks due to doping. This nonmonotonic evolution of the band gap with x explains the measured resistivity which shows the resistivity at low temperature maximizes around 40% of Ca doping (Fig. 11).

However, an interesting trend has been found in calculated spin and orbital magnetic moment as shown in Figs. 16 and 17, respectively, for the whole series ($x = 0$: SFIO; $x = 1$: CFIO). From Fig. 16(c) it is very clear that the Fe spin magnetic moments are mainly aligned along z component, while the m_x and m_y components [Figs. 16(a) and 16(b)] are very small compared to m_z component. Also, it shows that in spite of Ca doping the m_z component of Fe spin moment remains almost unchanged ($\sim 4.29 \mu_B$/site) across the series. On the other side, Ir spin moments for $x = 0$ (i.e., SFIO) are mainly concentrated in m_x component with small contribution of m_y component while almost nothing comes in m_z component. Therefore, for SFIO the Fe and Ir spins directions are orthogonal to each other. As the Ca concentration increases, the four Ir/Fe sites became inequivalent which results in an
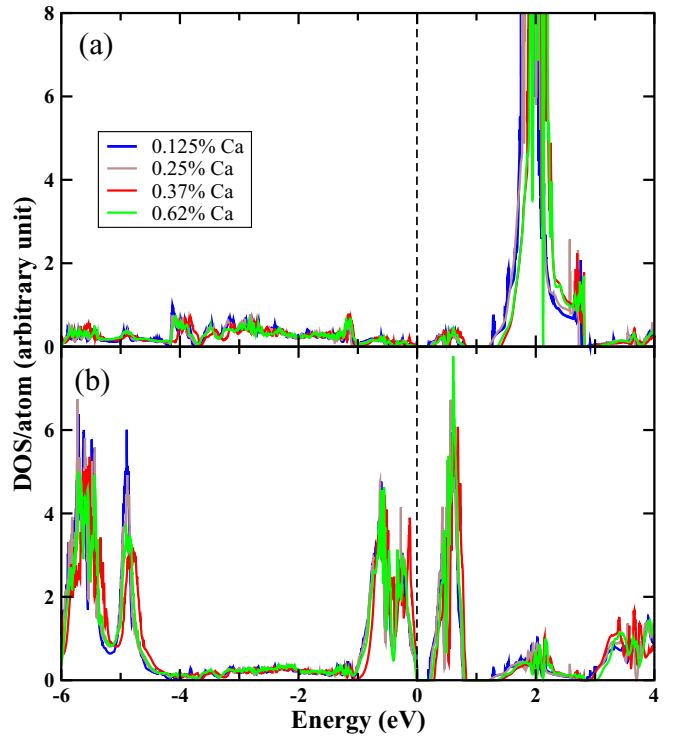

FIG. 15. (a) Fe-3d and (b) Ir-5d electronic DOS, calculated under GGA + U + SOC scheme for AFM state, are shown for $(Sr_{1-x}Ca_x)_2FeIrO_6$ series with the composition (x) mentioned in the plot. The Fermi energy is set at zero in the energy scale.

unequal development of moments at each site both in terms of magnitude and changing the sign. However, the effects are more prominent in the case of Ir than Fe due to its prominent SOC effect. For CFIO ($x = 1$), the Ir spin moment are concentrated both in m_x and m_z components, lying in xz plane. The orbital magnetic moment variation across the Ca
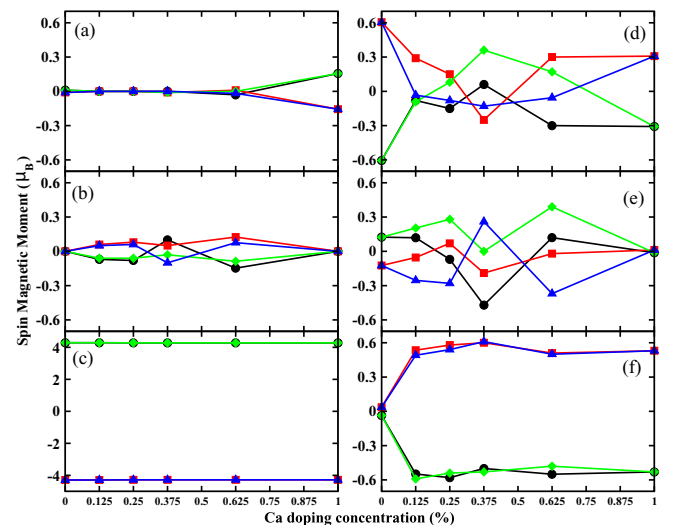

FIG. 16. The spin magnetic moment calculated under GGA + U + SOC [001] for AFM state are shown for (a) Fe-m_x, (b) Fe-m_y, (c) Fe-m_z, (d) Ir-m_x, (e) Ir-m_y, and (f) Ir-m_z across the $(Sr_{1-x}Ca_x)_2FeIrO_6$ series.
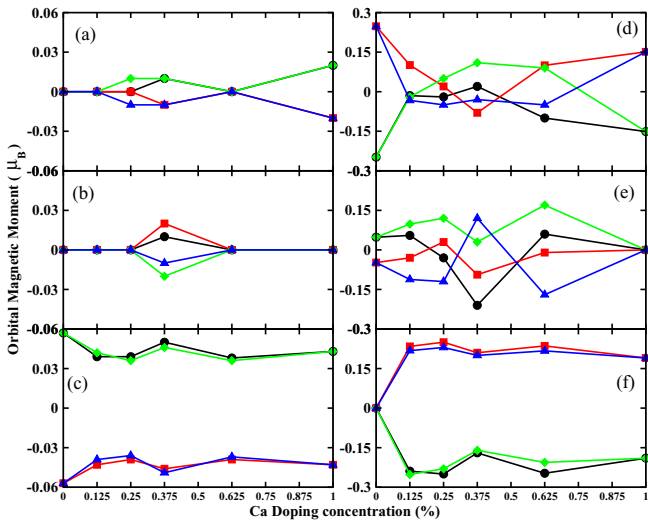
FIG. 17. The orbital magnetic moment calculated under GGA + U + SOC [001] for AFM state are shown for (a) Fe-o_x, (b) Fe-o_y, (c) Fe-o_z, (d) Ir-o_x, (e) Ir-o_y, and (f) Ir-o_z across the $(Sr_{1-x}Ca_x)_2FeIrO_6$ series.

doping has been shown in Fig. 17. The point to be mentioned here is that the orbital magnetic moments at Fe sites are very small (~ 0.06 μ_B/site) compared to that of the Ir site (~ 0.24 μ_B/site), which is expected due to the quenching of orbital degrees of freedom in Fe. However, the evolution of orbital magnetic moment with Ca doping follows a very similar trend as that of the spin magnetic moment (see Fig. 16). Similar to the spin moment, the Ir orbital moment for SFIO also shows major contribution along the m_x direction and for CFIO it lies in m_x and m_z directions as shown in Figs. 17(d), 17(e), and 17(f), respectively.

All the above GGA + U + SOC calculations with spin quantization axis along [001] direction hint for a strong magnetocrystalline anisotropy in these materials. Therefore, we have done a total energy comparison along different spin quantization axes for both SFIO and CFIO. Our results show that SFIO favors an easy-axis ([001] and [100] are degenerate in energy) kind of magnetocrystalline anisotropy (~ 1.61 meV/f.u.), whereas CFIO favors a [110] easy-plane kind of magnetocrystalline anisotropy (2.52 meV/f.u.). The calculated spin quantization results quite agree with the neutron diffraction measurements as shown in Fig. 10(c). In the [001] spin quantized ground state configuration of SFIO, all the Fe moments (spin + orbital) point along the z direction, however, the Ir moments (spin + orbital) remain orthogonal to that of Fe moment, directed mainly along x direction with a small component along y direction. One point need to be cleared here is that if we consider [100], then also Fe and Ir moments develop in the orthogonal direction, but then Fe and Ir spin moments aligned in the x and z direction, respectively. On the other hand, in the [110] spin quantized ground state of CFIO, the Fe and Ir spin moments are almost lying in xy plane (Fe-m_x = 3.04 μ_B/site, Fe-m_y = 3.02 μ_B/site, Ir-m_x = 0.43 μ_B/site, Ir-m_y = 0.46 μ_B/site), whereas the orbital moments for Ir are lying along the body the diagonal [111]

plane (Ir-o_x = 0.15 μ_B/site, Ir-m_y = 0.14 μ_B/site, Ir-m_z = 0.17 μ_B/site), as shown in Figs. 18(c) and 18(d).

These results can be visualized more clearly in the plot of magnetization density, as presented in Fig. 18. Point to be remembered here is that for plotting Fig. 18 we have chosen the lowest energy spin quantization axis for both SFIO (i.e., [001] degenerate with [100]) and CFIO (i.e., [110]) as discussed before, whereas in Figs. 16 and 17 the spin quantization axis is set to [001] for the whole series. For SFIO, Figs. 18(a) and 18(b) clearly show that Fe spin moments have only z component, whereas Ir moments have nothing in the z component but are completely concentrated in the x component. The shape of the Fe isosurface is almost spherically symmetric as expected for the half-filled d orbital (d^5) in $S = 5/2$ spin state. However, the shape of the Ir isosurface is distorted. For CFIO, the magnetization density along the m_x and m_y are plotted in Figs. 18(c) and 18(d), respectively. From the figure it is evident that in the case of CFIO, both Fe and Ir spin densities have almost similar contribution in both m_x and m_y component as discussed earlier, whereas the Fe and Ir spin moments are mainly concentrated in the x and z component. It is further observed that the shape of Fe isosurfaces are very similar in both cases of SFIO and CFIO, however, the shape of Ir isosurfaces vary significantly in both cases. The more distorted shape of the Ir isosurface in CFIO than SFIO indicates that the effective strength of SOC compared to crystal filed splitting and Coulomb correlation are substantially quenched in the case of CFIO due to enhanced octahedral distortion. Nonetheless, this evolution of magnetization density with Ca substitution or lattice distortion is quite intriguing.

V. DISCUSSION AND CONCLUSION

In summary, the solid state reaction method is used for the preparation of polycrystalline $(Sr_{1-x}Ca_x)_2FeIrO_6$ series with x from 0 to 1. The sample quality has been checked with XRD measurements and Rietveld analysis which suggest triclinic-$I\bar{1}$ structural symmetry is retained for the whole series, though the lattice parameters evolve with composition. Analysis of XPS data and electronic structure calculations suggest Sr/Ca is in 2+ nominal charge state while Fe/Ir retains its $3 + /5+$ nominal charge state throughout the series. Magnetization measurements suggest AFM spin ordering remain to be a low temperature magnetic state across the series though the transition temperature T_N decreases and other magnetic parameters exhibit anomalous behavior around $x = 0.2$. Temperature dependent neutron powder diffraction measurements reveal the triclinic-$I\bar{1}$ structural symmetry down to low temperature and confirm the magnetic Bragg peak at 5 K is related to AFM ordering where the site ordered moments for both Fe and Ir are observed, which has also been reconfirmed by the electronic structure total energy calculations. All the samples are found to be Mott type insulator where the charge transfer mechanism follows the 3D variable-range-hopping model.

The GGA + U + SOC electronic structure calculations reveal a detailed microscopic mechanism of the AFM-insulating state. We find that for the present investigated materials, there are strong competition among the SOC, electronic correlation (U), structural distortion, and bandwidth. As a result, the effective strength of SOC is reduced and it is not the
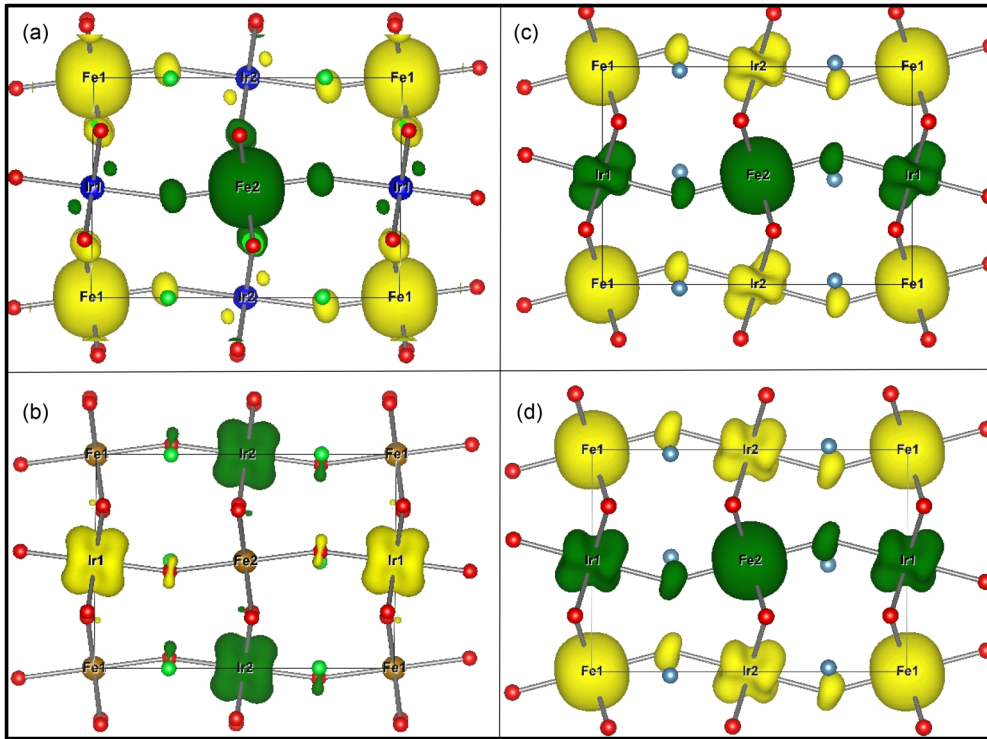
FIG. 18. The calculated magnetization density plot for AFM state with GGA $+ U +$ SOC scheme. The energetically favored spin quantization axes are chosen for each compounds, i.e., SFIO: [100] and CFIO : [110]. (a) and (b) The plot of z component (m_z) and x component (m_x) for SFIO, whereas (c) and (d) show similarly calculated m_x and m_y, respectively, for CFIO.

most dominating energy scale of the systems compared to other energy scales involved here. In conventional SOC-driven insulators, i.e., materials containing Ir^{4+} ($5d^5$) state [25–28,80,81], the orbital magnetic moment is as high as almost two times than the spin magnetic moment due to very high SOC. In the present systems, however, we find the orbital magnetic moment is lower than the spin magnetic moment (almost half), which indicates a considerably weaker strength of the effective SOC. Although the strength of SOC is an inherent atomic property, which does not change for a particular element in a particular electronic configuration, the comparative strength of the other energy scales such as U, bandwidth, and structural distortions dictate relative weightage in the final outcome. The present series of compounds are highly distorted and having large bandwidth (~ 1 eV) compared to the conventional SOC-driven insulating states found in other iridates (i.e., Sr_2IrO_4, $A_2Ir_2O_7$, Na_2IrO_3, etc.) [25–28,80,81]. Additionally, these double perovskites contain both $3d$ (Fe) and $5d$ (Ir) transition metals, hence an interplay between the electronic correlation and SOC as well as the narrow and extended wave functions plays a vital role in deciding their magnetic and electronic properties [25,26]. However, the SOC is an important energy scale here too, as it is very crucial in stabilizing the noncollinear AFM ground state with substantial anisotropy found in the calculations, but not the main energy scale of the system. Therefore, these materials belong to the intermediate region between the conventional electronic-correlation-driven Mott insulator and the conventional SOC-driven Mott insulator and can be classified as the SOC enhanced correlation-driven AFM-Mott insulator.

Our calculations further show SOC induced spin magnetic moment on Ir^{5+} (~ 0.62 μ_B/site) also agrees with the NPD experiments showing a site ordered moment of Ir (~ 0.5 μ_B). An indirect band gap between Γ and M point has been captured in band calculations which further increases with Ca doping. The calculations under GGA $+ U +$ SOC+AFM scheme show an interesting evolution of magnetic moment components (m_x, m_y, and m_z) of both Fe and Ir in the present series which mainly arises due to local structural distortion caused by lower size Ca^{2+} substitution. The calculated magnetization density further shows the deviation from ideal J_{eff} quantum number description of the electronic state due to the strong interplay among the SOC, structural distortion, and electron correlation in the present series of materials.

[1] J. Longo and R. Ward, J. Am. Chem. Soc. **83**, 2816 (1961).

[2] A. W. Sleight and J. F. Weiher, J. Phys. Chem. Solids **33**, 679 (1972).

[3] H. Yokoyama and T. Nakagawa, J. Phys. Soc. Jpn. **28**, 1197 (1970).

[4] D. Serrate, J. M. D. Teresa, and M. R. Ibarra, J. Phys. Condens. Matter **19**, 023201 (2007).

[5] S. Vasala and M. Karppinen, Prog. Solid State Chem. **43**, 1 (2014).

[6] J. Gopalakrishnan, A. Chattopadhyay, S. B. Ogale, T. Venkatesan, R. L. Greene, A. J. Millis, K. Ramesha, B. Hannoyer, and G. Marest, Phys. Rev. B **62**, 9538 (2000).

[7] P. D. Battle, T. C. Gibb, C. W. Jones, and F. Studer, J. Solid State Chem. **78**, 281 (1989).

[8] K. Nomura, R. Zboril, J. Tucek, W. Kosaka, S. Ohkoshi, and I. Felner, J. Appl. Phys. **102**, 013907 (2007).

[9] K. Naveen, M. Reehuis, P. Adler, P. Pattison, A. Hoser, T. K. Mandal, U. Arjun, P. K. Mukharjee, R. Nath, C. Felser, and A. K. Paul, Phys. Rev. B **98**, 224423 (2018).

[10] A. K. Paul, M. Reehuis, V. Ksenofontov, B. Yan, A. Hoser, D. M. Többens, P. M. Abdala, P. Adler, M. Jansen, and C. Felser, Phys. Rev. Lett. **111**, 167205 (2013).

[11] H. L. Feng, M. Arai, Y. Matsushita, Y. Tsujimoto, Y. Guo, C. I. Sathish, X. Wang, Y. H. Yuan, M. Tanaka, and K. Yamaura, J. Am. Chem. Soc. **136**, 3326 (2014).

[12] S. Kanungo, B. Yan, M. Jansen, and C. Felser, Phys. Rev. B **89**, 214414 (2014).

[13] G. Cao, S. McCall, M. Shepard, J. E. Crow, and R. P. Guertin, Phys. Rev. B **56**, 321 (1997).

[14] I. M. Gat-Malureanu, J. P. Carlo, T. Goko, A. Fukaya, T. Ito, P. P. Kyriakou, M. I. Larkin, G. M. Luke, P. L. Russo, A. T. Savici, C. R. Wiebe, K. Yoshimura, and Y. J. Uemura, Phys. Rev. B **84**, 224415 (2011).

[15] D. Fuchs, M. Wissinger, J. Schmalian, C.-L. Huang, R. Fromknecht, R. Schneider, and H. v. Löhneysen, Phys. Rev. B **89**, 174405 (2014).

[16] I. Terasaki, S. Shibasaki, S. Yoshida, and W. Kobayashi, Materials **3**, 786 (2010).

[17] C. Ma, H. X. Yang, L. J. Zeng, Y. Zhang, L. L. Wang, L. Chen, R. Xiong, J. Shi, and J. Q. Li, J. Phys. Condens. Matter **21**, 215606 (2009).

[18] G. Deng, N. Tsyrulin, P. Bourges, D. Lamago, H. Ronnow, M. Kenzelmann, S. Danilkin, E. Pomjakushina, and K. Conder, Phys. Rev. B **88**, 014504 (2013).

[19] Y. Liu, Z. Yang, H. Yang, T. Zou, Y. Xie, B. Chen, Y. Sun, Q. Zhan, and R. Li, J. Phys. D: Appl. Phys. **45**, 245001 (2012).

[20] S. Jia, A. J. Williams, P. W. Stephens, and R. J. Cava, Phys. Rev. B **80**, 165107 (2009).

[21] J. B. Philipp, P. Majewski, L. Alff, A. Erb, R. Gross, T. Graf, M. S. Brandt, J. Simon, T. Walther, W. Mader, D. Topwal, and D. D. Sarma, Phys. Rev. B **68**, 144431 (2003).

[22] A. E. Taylor, R. Morrow, R. S. Fishman, S. Calder, A. I. Kolesnikov, M. D. Lumsden, P. M. Woodward, and A. D. Christianson, Phys. Rev. B **93**, 220408(R) (2016).

[23] G. Chen, R. Pereira, and L. Balents, Phys. Rev. B **82**, 174440 (2010).

[24] Y. Krockenberger, K. Mogare, M. Reehuis, M. Tovar, M. Jansen, G. Vaitheeswaran, V. Kanchana, F. Bultmark, A. Delin, F. Wilhelm, A. Rogalev, A. Winkler, and L. Alff, Phys. Rev. B **75**, 020404(R) (2007).

[25] W. Witczak-Krempa, G. Chen, Y. B. Kim, and L. Balents, Annu. Rev. Condens. Matter Phys. **5**, 57 (2014).

[26] J. G. Rau, E. Kin-Ho Lee, and H.-Y. Kee, Annu. Rev. Condens. Matter Phys. **7**, 195 (2016).

[27] B. J. Kim, H. Jin, S. J. Moon, J. Y. Kim, B.-G. Park, C. S. Leem, J. Yu, T. W. Noh, C. Kim, S. J. Oh, J. H. Park, V. Durairaj, G. Cao, and E. Rotenberg, Phys. Rev. Lett. **101**, 076402 (2008).

[28] B. J. Kim, H. Ohsumi, T. Komesu, S. Sakai, T. Morita, H. Takagi, and T. Arima, Science **323**, 1329 (2009).

[29] K. C. Kharkwal and A. K. Pramanik, J. Phys. Condens. Matter **29**, 495801 (2017).

[30] D. Wallace and T. M. McQueen, Dalton Trans. **44**, 20344 (2015).

[31] A. Nag, S. Middey, S. Bhowal, S. K. Panda, R. Mathieu, J. C. Orain, F. Bert, P. Mendels, P. G. Freeman, M. Mansson, H. M. Ronnow, M. Telling, P. K. Biswas, D. Sheptyakov, S. D. Kaushik, V. Siruguri, C. Meneghini, D. D. Sarma, I. Dasgupta, and S. Ray, Phys. Rev. Lett. **116**, 097205 (2016).

[32] A. Biffin, R. D. Johnson, I. Kimchi, R. Morris, A. Bombardi, J.G. Analytis, A. Vishwanath, and R. Coldea, Phys. Rev. Lett. **113**, 197201 (2014).

[33] S. Kanungo, K. Mogare, B. Yan, M. Reehuis, A. Hoser, C. Felser, and M. Jansen, Phys. Rev. B **93**, 245148 (2016).

[34] M. M. Sala, K. Ohgushi, A. Al-Zein, Y. Hirata, G. Monaco, and M. Krisch, Phys. Rev. Lett. **112**, 176402 (2014).

[35] G. Cao, T. F. Qi, L. Li, J. Terzic, S. J. Yuan, L. E. DeLong, G. Murthy, and R. K. Kaul, Phys. Rev. Lett. **112**, 056402 (2014).

[36] B. Ranjbar, E. Reynolds, P. Kayser, and B. J. Kennedy, Inorg. Chem. **54**, 10468 (2015).

[37] T. Dey, A. Maljuk, D. V. Efremov, O. Kataeva, S. Gass, C. G. F. Blum, F. Steckel, D. Gruner, T. Ritschel, A. U. B. Wolter, J. Geck, C. Hess, K. Koepernik, J. van den Brink, S. Wurmehl, and B. Büchner, Phys. Rev. B **93**, 014434 (2016).

[38] B. F. Phelan, E. M. Seibel, D. B. Jr., W. Xie, and R. J. Cava, Solid State Commun. **236**, 37 (2016).

[39] M. Kusch, V. M. Katukuri, N. A. Bogdanov, B. Büchner, T. Dey, D. V. Efremov, J. E. Hamann-Borrero, B. H. Kim, M. Krisch, A. Maljuk, M. M. Sala, S. Wurmehl, G. Aslan-Cansever, M. Sturza, L. Hozoi, J. van den Brink, and J. Geck, Phys. Rev. B **97**, 064421 (2018).

[40] B. H. Kim, D. V. Efremov, and J. van den Brink, Phys. Rev. Mater. **3**, 014414 (2019).

[41] R. D. Shannon, Acta Crystallogr. Sect. A **32**, 751 (1976).

[42] P. D. Battle, G. R. Blake, T. C. Gibb, and J. F. Vente, J. Solid State Chem. **145**, 541 (1999).

[43] I. Qasim, P. E. R. Blanchard, S. Liu, C. Tang, B. J. Kennedy, M. Avdeev, and J. A. Kimpton, J. Solid State Chem. **206**, 242 (2013).

[44] L. Bufaiçal, C. Adriano, R. L. Serrano, J. G. S. Duque, L. M. Ferreira, C. R. Ayala, E. B. Saitovitch, E. M. Bittar, and P. G. Pagliuso, J. Solid State Chem. **212**, 23 (2014).

[45] P. Kayser, J. A. Alonso, F. J. Mompean, M. Retuerto, M. Croft, A. Ignatov, and M. T. F. Diaz, Eur. J. Inorg. Chem. **2015**, 5027 (2015).

[46] M. A. Laguna-Marco, P. Kayser, J. A. Alonso, M. J. Martinez-Lope, M. van Veenendaal, Y. Choi, and D. Haskel, Phys. Rev. B **91**, 214433 (2015).

[47] A. K. Paul, M. Jansen, B. Yan, C. Felser, M. Reehuis, and P. M. Abdala, Inorg. Chem. **52**, 6713 (2013).

[48] R. Morrow, R. Mishra, O. D. Restrepo, M. R. Ball, W. Windl, S. Wurmehl, U. Stockert, B. Büchner, and P. M. Woodward, J. Am. Chem. Soc. **135**, 18824 (2013).

[49] FULLPROF suite, http://www.ill.eu/sites/fullprof/.

[50] G. Kresse and J. Hafner, Phys. Rev. B **47**, 558(R) (1993); G. Kresse and J. Furthmuller, *ibid.* **54**, 11169 (1996).

[51] J. P. Perdew, K. Burke, and M. Ernzerhof, Phys. Rev. Lett. **77**, 3865 (1996).

[52] S. L. Dudarev, G. A. Botton, S. Y. Savrasov, C. J. Humphreys, and A. P. Sutton, Phys. Rev. B **57**, 1505 (1998).

[53] V. I. Anisimov, I. V. Solovyev, M. A. Korotin, M. T. Czyzyk, and G. A. Sawatzky, Phys. Rev. B **48**, 16929 (1993).

[54] N. Narayanan, D. Mikhailova, A. Senyshyn, D. M. Trots, R. Laskowski, P. Blaha, K. Schwarz, H. Fuess, and H. Ehrenberg, Phys. Rev B **82**, 024403 (2010).

[55] G. Cao, A. Subedi, S. Calder, J.-Q. Yan, J. Yi, Z. Gai, L. Poudel, D. J. Singh, M. D. Lumsden, A. D. Christianson, B. C. Sales, and D. Mandrus, Phys. Rev. B **87**, 155136 (2013).

[56] W. K. Zhu, J.-C. Tung, W. Tong, L. Ling, M. Starr, J. M. Wang, W. C. Yang, Y. Losovyj, H. D. Zhou, Y. Q. Wang, P.-H. Lee, Y.-K. Wang, C.-K. Lu, and S. X. Zhang, arXiv:1608.07763.

[57] V. Celorrio, L. Calvillo, G. Granozzi, A. E. Russell, and D. J. Fermin, Top. Catal. **61**, 154 (2018).

[58] H. V. Doveren and J. A. T. Verhoeven, J. Electron. Spectrosc. Relat. Phenom. **21**, 265 (1980).

[59] X. Liu, Y. Cao, B. Pal, S. Middey, M. Kareev, Y. Choi, P. Shafer, D. Haskel, E. Arenholz, and J. Chakhalian, Phys. Rev. Mater. **1**, 075004 (2017).

[60] P. C. Rogge, R. U. Chandrasena, A. Cammarata, R. J. Green, P. Shafer, B. M. Lefler, A. Huon, A. Arab, E. Arenholz, H. N. Lee, T.-L. Lee, S. Nemšák, J. M. Rondinelli, A. X. Gray, and S. J. May, Phys. Rev. Mater. **2**, 015002 (2018).

[61] M. Ghaffari, H. Huang, O. K. Tanaand, and M. Shannon, CrystEngComm **14**, 7487 (2012).

[62] T. Tsuyama, T. Matsuda, S. Chakraverty, J. Okamoto, E. Ikenaga, A. Tanaka, T. Mizokawa, H. Y. Hwang, Y. Tokura, and H. Wadati, Phys. Rev. B **91**, 115101 (2015).

[63] T. Yamashita and P. Hayes, App. Surf. Sci. **254**, 2441 (2008).

[64] A. P. Grosvenor, B. A. Kobe, M. C. Biesinger, and N. S. McIntyre, Surf. Interface Anal. **36**, 1564 (2004).

[65] M. Mullet, V. Khare, and C. Ruby, Surf. Interface Anal. **40**, 323 (2008).

[66] M. C. Biesingera, B. P. Paynec, A. P. Grosvenord, L. W. M. Laua, A. R. Gersonb, and R. S. C. Smartb, Appl. Surf. Sci. **257**, 2717 (2011).

[67] S. Fuentes, P. Munoz, N. Barraza, E. C. Angel, and C. M. S. Torres, J. Sol-Gel Sci. Technol. **75**, 593 (2015).

[68] W. K. Zhu, M. Wang, B. Seradjeh, F. Yang, and S. X. Zhang, Phys. Rev. B **90**, 054419 (2014).

[69] I. N. Bhatti, R. S. Dhaka, and A. K. Pramanik, Phys. Rev. B **96**, 144433 (2017).

[70] H. Kumar, R. S. Dhaka, and A. K. Pramanik, Phys. Rev. B **95**, 054415 (2017).

[71] T. Otsubo, S. Takase, and Y. Shimizu, ECS Transactions **3**, 263 (2006).

[72] G. Cao, V. Durairaj, S. Chikara, L. E. DeLong, S. Parkin, and P. Schlottmann, Phys. Rev. B **76**, 100402(R) (2007).

[73] A. Arrott, Phys. Rev. **108**, 1394 (1957).

[74] P. Kayser, M. J. Martínez-Lope, J. A. Alonso, M. Retuerto, M. Croft, A. Ignatov, and M. T. Fernández-Díaz, Inorg. Chem. **52**, 11013 (2013).

[75] J. Chen, H. J. Qin, F. Yang, J. Liu, T. Guan, F. M. Qu, G. H. Zhang, J. R. Shi, X. C. Xie, C. L. Yang, K. H. Wu, Y. Q. Li, and L. Lu, Phys. Rev. Lett. **105**, 176602 (2010).

[76] H.-T. He, G. Wang, T. Zhang, I.-K. Sou, G. K. L. Wong, J.-N. Wang, H.-Z. Lu, S.-Q. Shen, and F.-C. Zhang, Phys. Rev. Lett. **106**, 166805 (2011).

[77] M. Jenderka, J. Barzola-Quiquia, Z. Zhang, H. Frenzel, M. Grundmann, and M. Lorenz, Phys. Rev. B **88**, 045111 (2013).

[78] V. L. Nguyen, B. Z. Spivak, and B. I. Shklovskii, Zh. Eksp. Teor. Fiz. **89**, 1770 (1985) [Sov. Phys. JETP **62**, 1021 (1985)].

[79] N. Mott, *Conduction in Non-crystalline Materials* (Clarendon, Oxford, 1993).

[80] Y. Singh and P. Gegenwart, Phys. Rev. B **82**, 064412 (2010).

[81] D. Pesin and L. Balents, Nat. Phys. **6**, 376 (2010).

[82] J. B. Goodenough, Phys. Rev **100**, 564 (1955).

[83] J. Kanamori, J. Phys. Chem. Solids **10**, 87 (1959).